Sensing of Arbitrary-Frequency Fields Using a Quantum Mixer

Featured in Physics

Sensing of Arbitrary-Frequency Fields Using a Quantum Mixer

Guoqing Wang (王国庆),[1,*] Yi-Xiang Liu (刘仪襄),[1] Jennifer M. Schloss,[2] Scott T. Alsid,[1,2] Danielle A. Braje,[2] and Paola Cappellaro[1,3,†]

[1]*Research Laboratory of Electronics and Department of Nuclear Science and Engineering, Massachusetts Institute of Technology, Cambridge, Massachusetts 02139, USA*
[2]*Lincoln Laboratory, Massachusetts Institute of Technology, Lexington, Massachusetts 02421, USA*
[3]*Department of Physics, Massachusetts Institute of Technology, Cambridge, Massachusetts 02139, USA*

(Received 28 December 2021; revised 8 April 2022; accepted 5 May 2022; published 17 June 2022)

Quantum sensors such as spin defects in diamond have achieved excellent performance by combining high sensitivity with spatial resolution. Unfortunately, these sensors can only detect signal fields with frequency in a few accessible ranges, typically low frequencies up to the experimentally achievable control field amplitudes and a narrow window around the sensors' resonance frequency. Here, we develop and demonstrate a technique for sensing arbitrary-frequency signals by using the sensor qubit as a quantum frequency mixer, enabling a variety of sensing applications. The technique leverages nonlinear effects in periodically driven (Floquet) quantum systems to achieve quantum frequency mixing of the signal and an applied bias ac field. The frequency-mixed field can be detected using well-developed sensing techniques such as Rabi and CPMG with the only additional requirement of the bias field. We further show that the frequency mixing can distinguish vectorial components of an oscillating signal field, thus enabling arbitrary-frequency vector magnetometry. We experimentally demonstrate this protocol with nitrogen-vacancy centers in diamond to sense a 150-MHz signal field, proving the versatility of the quantum mixer sensing technique.

DOI: 10.1103/PhysRevX.12.021061 Subject Areas: Quantum Information

I. INTRODUCTION

From environmental noise in qubit platforms [1–3] to magnetism in condensed matter physics [4] and microwave antennas [5–7], magnetic fields of interest span from dc to GHz ranges. Quantum sensors such as neutral atoms [8–10], trapped ions [11], and solid-state spins [12,13] have made rapid progress in performance, yet have been limited to standard sensing protocols, including Rabi oscillation [14–17], and pulsed [18–21] and mixed dynamical decoupling [22]. These protocols severely limit the range of accessible frequencies to a narrow window around the sensor's resonance frequency or a low-frequency range constrained by the control field amplitude. For example, the accessible frequency range for solid-state nitrogen-vacancy (NV) spins in diamond [23] is currently limited to a near-resonant window around 2.87-GHz zero-field splitting or below a few MHz. Notably, NV ensembles have not yet been able to sense intermediate frequencies (50 MHz to 2 GHz) or ultrahigh frequencies (above a few GHz) because of the challenges of achieving large static fields and strong driving with the required homogeneity. Even for single defects, avoiding large static fields while achieving arbitrary-frequency *vector* magnetometry is desirable.

A strategy to overcome this constraint is to convert the desired signal to the accessible frequency range of preexisting sensing protocols by classical frequency mixers [24]. However, these bulky devices can be an obstacle to deploy quantum sensors and reduce their spatial resolution.

In this paper, we develop an integrated sensor and frequency mixer based on the same quantum device by exploiting virtual transitions between different Fourier manifolds in periodically driven (Floquet) quantum systems. This creates the quantum analog of a frequency mixer, which we dub quantum frequency mixing.

The synthetic ladder energy structure of Floquet systems [25] yields rich dynamics and broad applications [26]. In quantum simulations, Floquet systems have become versatile platforms for creating and characterizing exotic states of matter such as time crystals [27,28], topological phases [29–35], and quantum chaos [36], and Floquet states have been exploited to characterize dynamical symmetries [37,38], observe stimulated Raman transition [39], and simulate long-range hopping [40]. In quantum metrology,

*gq_wang@mit.edu
†pcappell@mit.edu

Floquet spectroscopy has been developed to sense ac magnetic field signals [20] and analyze spin systems [41]. For example, Floquet systems can be used to amplify weak signals by engineering spin-based masers [42,43], with applications in dark matter searches [44,45]. When driving with incompatible frequencies, the Floquet ladder structure extends into higher dimensions, leading to even more intriguing applications such as topological frequency conversion [46–48]. Under multiple driving frequencies, the dynamics of the quantum systems can be solved by multimode Floquet theory [49–52]. However, most multimode Floquet methods only analyze zero-frequency (on-resonance) terms, which give rise to static effective Hamiltonians. In this paper, we construct a theoretical framework based on Floquet theory to derive an effective frequency-mixed time-dependent Hamiltonian. This framework allows us to identify the frequency modes that dominate the dynamics and thus to build optimized protocols for frequency-mixer-based quantum sensing.

Importantly, our technique exploits well-known sensing protocols, such as continuous (Rabi) and pulsed dynamical decoupling, and expands these methods to a broader range of frequencies via quantum frequency mixing. Moreover, we extend our technique to enable arbitrary-frequency vector magnetometry by taking advantage of differences in the frequency conversions of transverse and longitudinal signal components. We demonstrate ac vector magnetometry exploiting nitrogen-vacancy centers in diamond. Quantum frequency mixing not only broadens the capabilities of quantum sensing, especially in extending the frequency range, but also opens up more potential applications.

This paper is organized as follows. In Sec. II, we give an intuitive picture of the main results of this work, including the principle of quantum frequency mixing and its application for quantum sensing. In Sec. III, we derive the effective Hamiltonian of quantum frequency mixing. In Sec. IV, we propose the protocol for sensing either transverse or longitudinal signal fields with an arbitrary frequency. In Sec. V, we discuss the strategy to improve sensitivities of these sensing protocols. In Sec. VI, we propose the principle for arbitrary-frequency vector ac magnetometry and perform a proof-of-principle experiment with a NV center ensemble, where we also characterize the sensitivity and discuss its limitations. In Sec. VII, we discuss more potential applications and summarize the paper.

II. PRINCIPLE OF QUANTUM MIXER

Frequency mixing is commonly used in classical electronics, where a frequency mixer or a multiplier generate the sum and difference of the original frequencies via a nonlinear electrical circuit [24]. The frequency conversion brings a signal to the optimal operational range of a device, allowing more efficient amplification, transmission, or detection, and it remains a dominant feature of radio reception and high-frequency oscilloscopes [24,53]. In quantum engineering, a classical frequency mixer up-converts the control fields to the resonance frequency of quantum devices to implement the desired quantum gates [1,54]. In addition, the frequency conversion based on general nonlinear effects in different materials [55–58] is also useful for optical engineering [59,60], quantum computation [61], quantum communication [62–64], and quantum sensing [65].

Thus, one natural idea to probe a signal with a frequency inaccessible by existing sensing protocols for a given quantum sensor (usually a high-frequency one) is to down-convert it by mixing with a bias ac field. However, existing (classical) frequency mixing methods are challenging in the context of quantum sensing, where the target signal might be localized at the nanoscale (and should be probed with a corresponding spatial resolution) or it is itself quantum in nature: In either scenario, mixing with a (bulky) classical apparatus might not be possible. We tackle this challenge by introducing quantum frequency mixing in quantum systems under multiple driving frequencies, as summarized with a simple schematic in Fig. 1(a). The idea is inspired by two-photon transitions mediated by an extra state coupled to two levels of the qubit sensor [66], but here we exploit a state in the Floquet space as the virtual level. When mapping these transitions back to the Hilbert

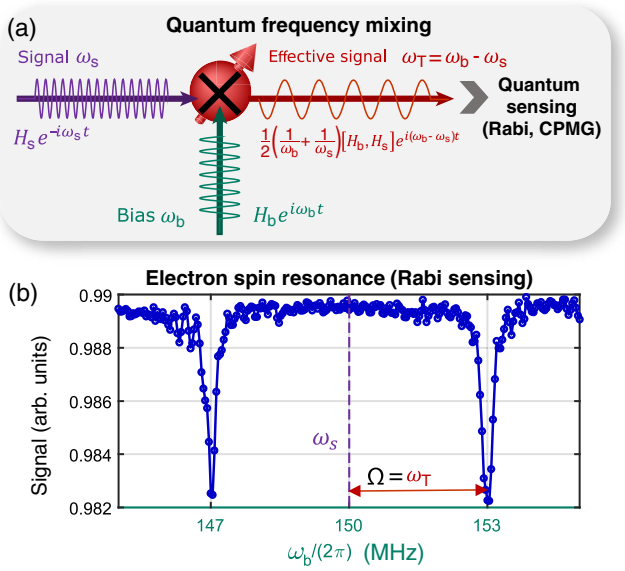

FIG. 1. (a) Quantum frequency mixing schematic. The effective Hamiltonian (red) emerges from the frequency mixing of the signal (purple) and bias (green) Hamiltonians. The effective Hamiltonian frequency ω_T can be probed experimentally. (b) Electron spin resonance (ESR) experiment to probe ω_T using an ensemble of NV centers. We sweep the bias field frequency ω_b to detect the presence of a signal field at $\omega_s = (2\pi)150$ MHz, which is not in the accessible range of typical sensing methods. We observe a resonance when the down-converted frequency $\omega_T = \pm(\omega_s - \omega_b)$ matches the probing drive amplitude at $\Omega = (2\pi)3$ MHz.

space, we find that the joint effect of two Fourier components $H_b e^{i\omega_b t}$ and $H_s e^{-i\omega_s t}$ in the system Hamiltonian is equivalent to an effective Hamiltonian with a frequency $\omega_b - \omega_s$.

Based on the theory of quantum frequency mixing, we propose a protocol for quantum sensing with an arbitrary-frequency range. Given a signal with frequency ω_s, we apply a bias field with frequency ω_b to convert the signal to a new target frequency $\omega_T = \omega_b - \omega_s$, which is in the accessible frequency range of preexisting sensing protocols, as shown in Fig. 1(a). Then, the frequency-converted signal can be probed by well-known methods in ac quantum sensing, including pulsed dynamical decoupling [12] or continuous decoupling [15,67] (by detecting Rabi oscillations [14] of either a population or a spin-locked state [15,68]).

Figure 1(b) shows a simple experimental demonstration of sensing via quantum frequency mixing with the Rabi method using an ensemble of electronic spin qubits based on NV centers in diamond. We assume that the achievable Rabi amplitude is $\Omega = (2\pi)3$ MHz at the qubit frequency $\omega_0 = (2\pi)2.2$ GHz, making it impossible to detect a 150-MHz transverse signal directly. However, when we simultaneously apply a bias field and sweep its frequency ω_b, we can observe an electron spin resonance when $\omega_b - \omega_s = \pm\Omega$, demonstrating that we induced a down-converted signal at frequency $\omega_T = \omega_b - \omega_s$.

While it is easy to grasp the intuitive picture of quantum sensing via quantum frequency mixing, evaluating its performance and designing the most effective protocols requires a more in-depth analysis of the dynamics, which can be obtained by developing a modified multimode Floquet theory. This more comprehensive picture further provides insights enabling the development of a protocol for arbitrary-frequency vector magnetometry.

III. MULTIMODE FLOQUET THEORY

In this section, we extend multimode Floquet theory to derive a time-dependent effective Hamiltonian arising from the mixing of different frequency modes. The precision of the analytical approximation is then evaluated by numerically characterizing the evolution of a qubit under two driving frequencies.

A. Theory

The dynamics of time-periodic Hamiltonians can be solved by Floquet theory [25], where a time-dependent Schrödinger equation $i(\partial/\partial t)\Psi(t) = H(t)\Psi(t)$ is simplified to a time-independent, infinite-dimensional, Floquet matrix problem $H_F\Phi = \lambda\Phi$. Here, λ is the eigenvalue of the Floquet matrix representing the eigenenergy, and Φ is the eigenvector comprised of Fourier components of eigenstates $\Phi(t)$ satisfying $\Psi(t) = e^{-i\lambda t}\Phi(t)$. Besides fully diagonalizing the Floquet matrix (with proper matrix truncation) to numerically obtain the dynamics, the Floquet-space evolution can be analyzed via time-independent perturbation theory to highlight the contributions of frequencies of interest [49–51]. However, these analytical methods are typically constrained to zero-frequency (on-resonance) terms. Alternate approaches to obtain time-dependent effective Hamiltonians such as the Jacobi-Anger expansion [69] require complicated analysis, limiting their application in quantum sensing.

Here, we extend the perturbation theory approach such that the nonstatic effective Hamiltonian due to the mixing of different frequency modes can also be analyzed. In comparison to typical perturbation theory methods where higher-order Hamiltonian corrections arise from virtual transitions through intermediate energy levels, here the higher-order terms correspond to virtual transitions between different Fourier manifolds in the multimode Floquet space, which then give rise to frequency mixing between different modes.

We start with a bimodal Floquet problem. For a periodically driven quantum system with two frequency modes (ω_q, ω_r), the Fourier expansion of the Hamiltonian in Hilbert space is

$$H(t) = \sum_{n=-\infty}^{\infty}\sum_{k=-\infty}^{\infty} H^{(n,k)} e^{in\omega_q t} e^{ik\omega_r t}, \tag{1}$$

where $H^{(n,k)} = (H^{(-n,-k)})^\dagger$ because the Hamiltonian $H(t)$ is Hermitian and (n,k) denotes the frequency order. When expressed in the bimodal Floquet space, the Hamiltonian becomes a time-independent Floquet Hamiltonian,

$$H_F = \sum_{n=-\infty}^{\infty}\sum_{k=-\infty}^{\infty} H^{(n,k)} \otimes F_n^q \otimes F_k^r + \omega_q F_z^q + \omega_r F_z^r, \tag{2}$$

by introducing the ladder operator $F_n = \sum_m |m+n\rangle\langle m|$, representing a hopping process from $|m\rangle$ to $|m+n\rangle$ in the corresponding dimension in Floquet space, and the number operator $F_z = \sum_m m|m\rangle\langle m|$, representing the ladder energy [49–51]. In other words, the Fourier components give rise to equidistant energy levels (with energy differences $\omega_{q,r}$) in Floquet space [see Fig. 2(a)]. By applying a unitary transformation $U = e^S$ with S anti-Hermitian to block diagonalize the Floquet matrix H_F in Eq. (2) and then transforming back to the Hilbert space, we obtain an effective Hamiltonian $\bar{H}(t)$ describing the frequency-mixed dynamics of the system such that

$$\bar{H}(t) = \sum_{m,h}\left[H^{(m,h)} + H^{(m,h)}_{(2)} + \cdots\right] e^{i(m\omega_q + h\omega_r)t}, \tag{3}$$

where the second-order term is

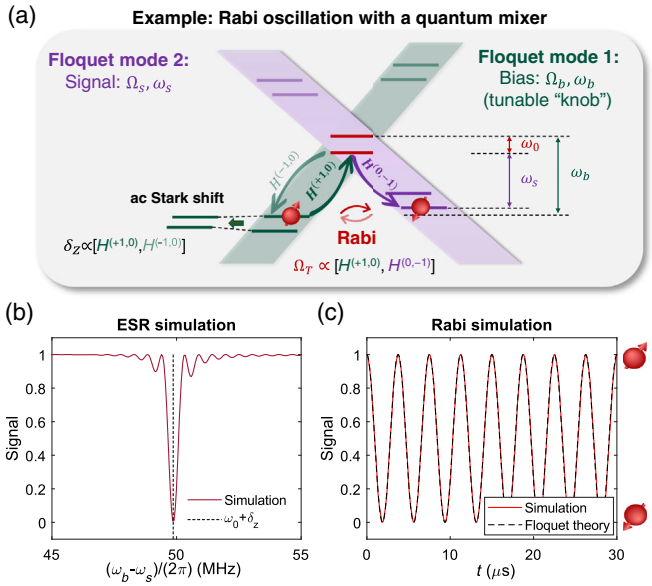

FIG. 2. Characterization of the effective Hamiltonian [Eq. (12)] predicted by Floquet theory, for a qubit of energy $\omega_0 = (2\pi)50$ MHz and a signal field with frequency $\omega_s = (2\pi)375$ MHz and amplitude $\Omega_{sz} = (2\pi)10$ MHz. To achieve quantum frequency mixing, we apply a bias field with $\Omega_b = \Omega_{sz}$. (a) Schematic showing the Rabi transition and the ac Stark shift mediated by the virtual Floquet states. (b) Qubit population in the $|0\rangle$ state at a fixed time $t = 1.875$ μs as a function of the bias field frequency. Similar to an electron spin resonance (ESR) experiment, we observe a resonance at $\omega_b - \omega_s = \omega_0 + \delta_z$ (marked by a dashed line). Note that the ac Stark shift here is obtained with a more precise analysis in the rotating frame such that $\delta_z/2 = \Omega_b^2/4(\omega_0 - \omega_b)$ (see Appendix B 1). (c) Population in $|0\rangle$ as a function of time, at the resonance condition. Similar to a Rabi experiment, we observe oscillations with a rate set by Ω_{Tz}.

$$H_{(2)}^{(m,h)} = -\frac{1}{2}\sum_{n,k}\frac{[H^{(m-n,h-k)}, H^{(n,k)}]}{n\omega_q + k\omega_r}, \tag{4}$$

with $n\omega_q + k\omega_r \neq 0$ (see a more detailed derivation in Appendix A). For a general multimode Floquet problem, all the results are valid by simply replacing the frequency modes (q, r) with $(q, r, s, \cdots)$.

Typically, the expansion in Eq. (3) is not only truncated to the lowest nonzero contribution but also to retain only the cross-resonance $m\omega_q + h\omega_r = 0$ terms, leading to a time-independent effective Hamiltonian when transforming back to Hilbert space [49–51]. In this work, we instead include all the modes (m, h) that dominate the system dynamics, neglecting only fast oscillation (in the spirit of the rotating wave approximation, or RWA):

$$m\omega_q + h\omega_r \ll \omega_l, \tag{5}$$

where $\omega_l \in \{n\omega_q + k\omega_r | n\omega_q + k\omega_r \neq 0, H^{(n,k)} \neq 0\}$ are all nonvanishing, high-frequency Fourier components of the Hamiltonian. Thus, we retain a broader set of distinct, mixed-up driving frequencies that determine the system dynamics.

The theoretical results up to second-order expansion can be summarized with a simple "mixer"-like schematic as shown in Fig. 1(a), which provides an intuitive picture for predicting and designing desired dynamics. The evolution of a quantum system under two unmixed Hamiltonian Fourier components $H_1 e^{i\omega_1 t}$ and $H_2 e^{i\omega_2 t}$ is equivalent—up to the second-order expansion—to the dynamics given by a "mixed" interaction with frequency $\omega_1 + \omega_2$, given by

$$H_1 e^{i\omega_1 t} + H_2 e^{i\omega_2 t} \Rightarrow \frac{1}{2}\left(\frac{1}{\omega_1} - \frac{1}{\omega_2}\right)[H_1, H_2] e^{i(\omega_1+\omega_2)t}. \tag{6}$$

For a general multimode problem, the effective Hamiltonian up to second order can be calculated by summing over mixed terms due to all frequency pairs, where each pair generates an effective mixed Hamiltonian according to Eq. (6).

B. Example

Assume we want to use a qubit sensor with energy ω_0 to detect a longitudinal signal field with Hamiltonian

$$H_{sz} = \Omega_{sz}\cos(\omega_s t)\sigma_z, \tag{7}$$

with a frequency ω_s that is outside the range accessible by the sensor. To convert the signal frequency, we apply a circularly polarized transverse bias field with Hamiltonian

$$H_b = \frac{\Omega_b}{2}[\cos(\omega_b t)\sigma_x + \sin(\omega_b t)\sigma_y]. \tag{8}$$

In the absence of the signal field ($\Omega_{sz} = 0$), the problem can be solved exactly in a rotating frame defined by $U = e^{-i(\omega_b t/2)\sigma_z}$, yielding a time-independent Hamiltonian $(\omega_0 - \omega_b)\sigma_z/2 + \Omega_b\sigma_x/2$. Note that for $\Omega_b \ll (\omega_0 - \omega_b)$, to first-order perturbation theory, this reduces to evolving under an energy shift $\Omega_b^2/[4(\omega_0 - \omega_b)]\sigma_z$ (the ac Stark shift) in the rotating frame. This simple approach cannot be used to analyze the effect of the signal field, which is still time dependent in the rotating frame, and we need Floquet theory to tackle the problem. The bimodal Floquet Hamiltonian—for modes (ω_b, ω_s)—is defined by the Fourier components in the lab frame,

$$H^{(0,0)} = \frac{\omega_0}{2}\sigma_z, \quad H^{(\pm1,0)} = \frac{\Omega_b}{2}\sigma_\mp, \quad H^{(0,\pm1)} = \frac{\Omega_{sz}}{2}\sigma_z, \tag{9}$$

with the operators $\sigma_\pm = (\sigma_x \pm i\sigma_y)/2$. Each of these components gives rise to transitions in the 2D energy-level ladder of Floquet space shown in Fig. 2(a). Note that $H^{(\pm1,0)}$ is associated with the hopping $F_{\pm1}^b$ in the first dimension, indicated by the green arrows, while $H^{(0,\pm1)}$ is

associated with hoppings in the second dimension, indicated by the purple arrow. Focusing on quasienergy-conserving second-order transitions, two effects emerge: the ac Stark shift and the Rabi driving. The ac Stark shift is due to transitions in the bias field space alone ($H^{(\pm 1,0)}$). Each transition changes the spin state (as they do not commute), but the whole process conserves energy [$\omega_1 = -\omega_2 = \omega_b$ in Eq. (6)], giving rise to a simple energy shift. Using Eq. (6), we can calculate

$$\bar{H}_{\delta_z} = \frac{1}{\omega_b}[H^{(1,0)}, H^{(-1,0)}] = -\frac{\Omega_b^2}{4\omega_b}\sigma_z = \frac{\delta_z}{2}\sigma_z, \tag{10}$$

where δ_z is the ac Stark shift due to the bias field. Note that the two hoppings $H^{(0,\pm 1)}$ do not introduce such a shift since they leave the spin state unchanged (that is, they commute). By exploiting transitions involving both Floquet dimensions (the bias and signal field), we can induce a flip in the qubit state, when $\omega_b - \omega_s \approx \omega_0$. These transitions, due to the two hoppings $H^{(1,0)}$, $H^{(0,-1)}$ and the Hermitian conjugate process, yield a Rabi driving given by

$$\begin{aligned}\bar{H}_\Omega &= \left[\frac{1}{2}\left(\frac{1}{\omega_b} + \frac{1}{\omega_s}\right)[H^{(1,0)}, H^{(0,-1)}]e^{i(\omega_b-\omega_s)t} + \text{H.c.}\right] \\ &= \Omega_{Tz}[\cos(\omega_T t)\sigma_x + \sin(\omega_T t)\sigma_y],\end{aligned} \tag{11}$$

where the mixed signal frequency is $\omega_T = \omega_b - \omega_s$, with an amplitude $\Omega_{Tz} = (\Omega_b\Omega_{sz}/4)({\omega_b}^{-1} + {\omega_s}^{-1})$. When neglecting fast oscillation terms in comparison to the energy gap ω_0, the effective Hamiltonian is given by

$$\bar{H} = \frac{\omega_0}{2}\sigma_z + \bar{H}_{\delta_z} + \bar{H}_\Omega. \tag{12}$$

We note that Eq. (6) applies to all frequency pairs, irrespective of their sign, and thus we should also consider terms proportional to $[H^{(1,0)}, H^{(0,1)}]$ that give rise to oscillations at $\omega_s + \omega_b$. However, these terms correspond to fast oscillations, i.e., $\omega_s + \omega_b \gg |\omega_T|, \omega_0$, and can be neglected in Eq. (12), leaving only the term oscillating at the target-sensing frequency. We also assume that the amplitudes Ω_b, Ω_{sz} are much smaller than the mode frequencies ω_b, ω_s, so the perturbation expansion can be truncated to second order. Appendix B 1 contains a detailed derivation and discussion of the optimal choice of reference frame.

The theoretical results in Eq. (12) can be validated by simulating the system dynamics, sweeping the bias frequency to determine ω_T and sweeping the time to determine Ω_{Tz}. Indeed, we expect the spin to evolve on resonance when $\omega_T = \omega_b - \omega_s = \omega_0 + \delta_z$, with a rate set by the effective Rabi amplitude Ω_{Tz}, as shown in Figs. 2(b) and 2(c), where we compare numerical simulations to the behavior predicted by the Hamiltonian $\bar{H}$ in Eq. (12).

IV. QUANTUM SENSING BY QUANTUM FREQUENCY MIXING

With an understanding of quantum frequency mixing, we can now devise various quantum-sensing protocols and analyze their performance. A broad overview of potential protocols is given in Table I, where we subdivide the various scenarios as follows: (1) longitudinal (commuting with the qubit sensor internal Hamiltonian) or transverse

TABLE I. Various quantum-sensing protocols based on quantum frequency mixing. All parameters are expressed in the rotating frame defined by $e^{-i(\omega t/2)\sigma_z}$ except for the signal and bias Hamiltonians, which are in the lab frame. The Bloch-Siegert shift $\Omega^2/(8\omega)$ and possible frequency mixing due to the spin-locking driving field in the Rabi measurement are neglected. In the notation of the polarization of the signal, the bias, and the target (mixed) signal, $\sigma_\pm$ denotes a circularly polarized field with the form $\Omega[\cos(\omega t)\sigma_x \pm \sin(\omega t)\sigma_y]$, and $\sigma_{z,x}$ denote linearly polarized longitudinal and transverse fields with the form $\Omega\cos(\omega t)\sigma_{z,x}$. We note that all frequency mixing terms potentially of use for quantum sensing are listed for completeness, and terms not satisfying the near-resonance condition in Eq. (5) are neglected in practical calculations. Detailed derivations are included in Appendix B.

	Protocol 1	Protocol 2	Protocol 3	Protocol 4	Protocol 5
Signal (ω_s, Ω_s)	σ_z	σ_z	σ_x	σ_x	σ_x
Bias (ω_b, Ω_b)	σ_x	σ_+	σ_x	σ_+	σ_z
Target (ω_T, Ω_T)	σ_+ or σ_-	σ_+	$-\sigma_z$	$-\sigma_z$	σ_+ or σ_-
ω_T	$\omega_b - \omega \pm \omega_s$ or $\omega_b + \omega \pm \omega_s$	$\omega_b - \omega \pm \omega_s$	$\omega_b - \omega_s$	$\omega_b - \omega_s$	$\omega_s - \omega \pm \omega_b$ or $\omega_s + \omega \pm \omega_b$
$\delta_z/2$	$-\frac{\Omega_b^2\omega}{2(\omega_b^2-\omega^2)}$	$-\frac{\Omega_b^2}{4(\omega_b-\omega)}$	$-\frac{\Omega_b^2\omega}{2(\omega_b^2-\omega^2)} - \frac{\Omega_{sx}^2\omega}{2(\omega_s^2-\omega^2)}$	$-\frac{\Omega_b^2}{4(\omega_b-\omega)} - \frac{\Omega_{sx}^2\omega}{2(\omega_s^2-\omega^2)}$	$-\frac{\Omega_{sx}^2\omega}{2(\omega_b^2-\omega^2)}$
Ω_T	$\frac{\Omega_{sz}}{4}(\frac{\Omega_b}{\omega_b-\omega} \mp \frac{\Omega_b}{\omega_s})$ or $-\frac{\Omega_{sz}}{4}(\frac{\Omega_b}{\omega_b+\omega} \mp \frac{\Omega_b}{\omega_s})$	$\frac{\Omega_{sz}}{4}(\frac{\Omega_b}{\omega_b-\omega} \mp \frac{\Omega_b}{\omega_s})$	$\frac{\Omega_{sx}}{2}(\frac{\Omega_b\omega}{\omega_b^2-\omega^2} + \frac{\Omega_b\omega}{\omega_s^2-\omega^2})$	$\frac{\Omega_{sx}}{4}(\frac{\Omega_b}{\omega_b-\omega} + \frac{\Omega_b}{\omega_s-\omega})$	$\frac{\Omega_{sx}}{4}(\frac{\Omega_b}{\omega_s-\omega} \mp \frac{\Omega_b}{\omega_b})$ or $-\frac{\Omega_{sx}}{4}(\frac{\Omega_b}{\omega_s+\omega} \mp \frac{\Omega_b}{\omega_b})$
$\epsilon = \Omega_T/\Omega_s$	$\Omega_b/(2\omega_s)$	$\Omega_b/(2\omega_s)$	$\Omega_b/\omega(\omega_s \ll \omega)$, $\Omega_b\omega/\omega_s^2(\omega_s \gg \omega)$	$\Omega_b/(2\omega)(\omega_s \ll \omega)$, $\Omega_b/(2\omega_s)(\omega_s \gg \omega)$	$\Omega_b/(2\omega_b)$

signal field; (2) longitudinal or transverse bias field with linear or circular polarization. For each of the viable combinations of these scenarios, we can use either continuous (Rabi) or pulsed (CPMG) sensing protocols to sense the effective signal at ω_T. In the following, we examine in detail two exemplary cases.

A. Example 1: Sensing of longitudinal signals by Rabi oscillations

We first describe the detection of a longitudinal signal with frequency ω_s [see Eq. (7)], where the goal is to determine the amplitude Ω_{sz}. Here, we use a qubit sensor with (internal) energy $H_0 = \omega_0\sigma_z/2$ and apply a circularly polarized bias H_b as described in Eq. (8). As shown in Appendix B 1 a, the analysis is better carried out in the rotating frame set by H_0, where the Hamiltonian $H = H_{sz} + \widetilde{H_b}$. Here, the modified bias term is

$$\widetilde{H_b} = \frac{\Omega_b}{2}[\cos(\tilde{\omega}_b t)\sigma_x + \sin(\tilde{\omega}_b t)\sigma_y], \tag{13}$$

where $\tilde{\omega}_b = \omega_b - \omega_0$ is the shifted bias frequency in the rotating frame. Under the assumptions $\tilde{\omega}_b - \omega_s$, $\Omega_{b,s} \ll \tilde{\omega}_b, \omega_s$, we retrieve the results of Sec. III B, finding an effective Hamiltonian $\bar{H}_I$ [Eq. (12)] with a target signal frequency $\omega_T = \omega_b - \omega_0 - \omega_s$ and amplitude

$$\Omega_{Tz} = \frac{\Omega_b\Omega_{sz}}{4}\left(\frac{1}{\omega_b - \omega_0} + \frac{1}{\omega_s}\right). \tag{14}$$

As simulated in Fig. 2, the effective target signal field can be used to drive the qubit evolution (Rabi oscillation) by setting $\omega_T = \delta_z = -\Omega_b^2/(2\tilde{\omega}_b)$ and thus estimate Ω_{sz}.

Since the typical Rabi oscillation of the population state $|0\rangle$ is limited by a short coherence time, a more robust sensing protocol is achieved by adding an additional driving field at frequency $\omega = \omega_0(+\delta_z)$ with amplitude Ω to perform Rabi sensing in the rotating frame [15,68,70], where the Rabi oscillation of an initial spin-locked state $|+\rangle$ is used to extract the target signal. Then, the target frequency ω_T can be simply set equal to Ω, and the component of the effective target signal field orthogonal to the spin-locking x direction will drive Rabi oscillations. More precisely, we prepare the system initial state to $|+\rangle$ and switch on a spin-locking microwave drive $(\Omega/2)[\cos(\omega t)\sigma_x + \sin(\omega t)\sigma_y]$, which is on resonance with the static energy $\omega = \omega_0$, while at the same time applying the target signal and bias fields. The effective Hamiltonian in the rotating frame is then simplified to

$$\bar{H}_I = \frac{\Omega}{2}\sigma_x + \Omega_{Tz}\sin[(\tilde{\omega}_b - \omega_s)t]\sigma_y, \tag{15}$$

where $\Omega_{Tz}, \delta_z \ll \Omega$, such that both the ac Stark shift and the effective target signal term along x in Eq. (12) are negligible. When the target signal frequency is on resonance with the static energy in the rotating frame $|\omega_b - \omega_0 - \omega_s| = \Omega$, a Rabi oscillation is induced, which can be obtained by monitoring the population of the initial state $|+\rangle$, yielding an oscillation signal $S(t)$:

$$S(t) = P_{|+\rangle}(t) = \frac{1}{2}[1 + \cos(\Omega_{Tz}t)]. \tag{16}$$

The field amplitude Ω_{sz} can then be extracted from the signal oscillation frequency Ω_{Tz} through Eq. (14).

We note that, even in the more common case where the bias field and spin-locking drive are both linearly polarized, we obtain the same effective target signal in the rotating frame, at the cost of additional ac Stark shifts and a Bloch-Siegert shift induced by the counterrotating terms of the bias and the spin-locking fields, respectively. These static shifts have small amplitudes in comparison to Ω and can be neglected (more details are included in both Table I and Appendix B 1).

B. Example 2: Sensing of transverse signals by pulsed dynamical decoupling

When the signal field is transverse, we can add either a longitudinal or a transverse bias field to achieve quantum frequency mixing. In the first case, the analysis is similar to that described above by switching the bias and signal fields, with results in Protocol 5 in Table I. Alternatively, we can apply the same transverse bias field as in Eq. (8).

Assume a transverse ac signal field couples to the qubit sensor with Hamiltonian

$$H_{sx} = \Omega_{sx}\cos(\omega_s t)\sigma_x. \tag{17}$$

Then, the Hamiltonian in the rotating frame with the bias field is $H_I = \tilde{H}_b + \tilde{H}_{sx}$, where $\tilde{H}_b$ is the same as Eq. (13) and $\tilde{H}_{sx}$ is

$$\begin{aligned}\tilde{H}_{sx} = &\frac{\Omega_{sx}}{2}[\cos(\tilde{\omega}_s t)\sigma_x + \sin(\tilde{\omega}_s t)\sigma_y] \\ &+ \frac{\Omega_{sx}}{2}[\cos(\tilde{\tilde{\omega}}_s t)\sigma_x - \sin(\tilde{\tilde{\omega}}_s t)\sigma_y]\end{aligned} \tag{18}$$

with shifted frequencies $\tilde{\omega}_s = \omega_s - \omega_0$ and $\tilde{\tilde{\omega}}_s = \omega_s + \omega_0$.

The dynamics under the Hamiltonian H_I can again be solved with our results in Eq. (6). Under the similar assumptions $\tilde{\omega}_b - \tilde{\omega}_s$, $\Omega_{b,s} \ll \tilde{\omega}_b, \tilde{\omega}_s, \tilde{\tilde{\omega}}_s$, the mode dominating the system dynamics is the frequency difference $\tilde{\omega}_b - \tilde{\omega}_s$, yielding the effective Hamiltonian

$$\bar{H}_I = \frac{\delta_z}{2}\sigma_z - \Omega_{Tx}\cos[(\omega_b - \omega_s)t]\sigma_z, \tag{19}$$

where the static ac Stark shift due to both the bias and signal fields is $\delta_z/2 = -(1/4)[\Omega_b^2/\tilde{\omega}_b + \Omega_s^2/\tilde{\omega}_s - \Omega_s^2/\tilde{\tilde{\omega}}_s]$, and Ω_{Tx} is the target signal amplitude,

$$\Omega_{Tx} = \frac{\Omega_b \Omega_{sx}}{4}\left(\frac{1}{\omega_b - \omega_0} + \frac{1}{\omega_s - \omega_0}\right). \quad (20)$$

The initial transverse signal is converted to a longitudinal signal with a (lower) frequency $\omega_T = \omega_b - \omega_s$ and a reduced amplitude Ω_{Tx}. While this effective target signal can be measured by the same rotating-frame Rabi protocol described above under the resonance condition $|\omega_b - \omega_s| = \Omega$, it also naturally lends itself to pulsed dynamical decoupling ac sensing methods [12]. Pulsed dynamical decoupling sequences such as CPMG [18,71] have previously been implemented in sensing both longitudinal [12,19,72] and transverse signals [20], where a series of π pulses is applied periodically with an interval τ and only frequencies on resonance with the pulse train lead to prominent state evolution. When $|\omega_b - \omega_s| = \pi/\tau$, the effective mixed signal in Eq. (19) is on resonance with the CPMG sequence. Then, the amplitude of the transverse component of the target signal can be obtained by measuring the population in initial state $|+\rangle$ as a function of the pulse number $N = t/\tau$, yielding

$$S(t) = P_{|+\rangle}(t) = \frac{1}{2}\left[1 + \cos\left(\frac{4\Omega_{Tx} t}{\pi}\right)\right]. \quad (21)$$

V. SENSITIVITY TO QUANTUM FREQUENCY-MIXED SIGNALS

In designing protocols for arbitrary-frequency (and direction) sensing, the goal is to achieve the optimal sensitivity, which is the minimally detectable field change per unit time. The sensitivity η to the signal amplitude Ω_s is given by $\eta = \sigma_S \sqrt{t + t_d}/(dS/d\Omega_s)$ [13], where $S(\Omega_s)$ is the measurement signal, σ_S is the signal uncertainty, and t, t_d are the sensing time and sequence dead time, respectively. By a careful choice of initial state and control protocol, the signal can always be written as

$$S = \frac{1}{2}[1 + e^{-\chi}\cos(\epsilon \Omega_s t)], \quad (22)$$

where the factor χ is due to the signal decay, and the factor ϵ sets the sensitivity degradation in comparison to typical protocols without frequency mixing. Both of the factors are dependent on the protocol chosen. In Table I, we review possible protocols for sensing transverse and longitudinal signals with quantum frequency mixing by different bias fields. Since the factor ϵ is shown to be proportional to the bias amplitude such that $\eta \propto 1/\Omega_b$, the sensitivity can be improved by increasing Ω_b.

To further validate the theoretically derived target signal amplitude and to explore the optimal sensitivity, we simulate the rotating-frame Rabi oscillations for the sensing of both longitudinal signals and transverse signals. The Fourier spectrum of the Rabi oscillations, together with the theoretical predictions, is shown in Fig. 3. In Figs. 3(a) and 3(b), we simulate the Rabi spectrum as a function of bias amplitude Ω_b. When the bias amplitude Ω_b is small, the simulation matches the linear dependence predicted by the theory with ac Stark shift terms neglected. When Ω_b is large, the simulated Rabi frequency deviates from a linear dependence on Ω_b because of the larger frequency detuning caused by the ac Stark shifts, and the simulation matches the theoretical prediction when such shifts δ_z are taken into account.

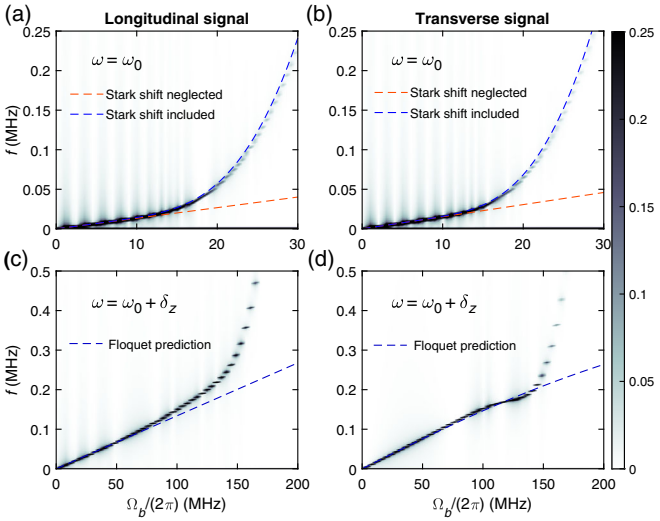

FIG. 3. Bias amplitude sweep. (a) Bias amplitude sweep for longitudinal signal sensing. The intensity plot is the Fourier spectrum of the Rabi signal $P_{|+\rangle}(t)$ under different bias amplitudes Ω_b. The transverse bias field is circularly polarized (same for other panels). The signal and bias frequencies are fixed at $\omega_s = (2\pi)375$ MHz and $\omega_b = \omega_s + \omega_0 - \Omega$. The signal and spin-locking drive amplitudes are $\Omega_{sz} = (2\pi)1$ MHz and $\Omega = (2\pi)3$ MHz, and the spin-locking drive frequency is on resonance with the qubit frequency $\omega = \omega_0 = (2\pi)50$ MHz. Dashed lines are theoretical predictions. (b) Bias amplitude sweep for transverse signal sensing. The parameters are similar to panel (a) except for the resonance condition $\omega_b = \omega_s + \Omega$ and signal amplitude $\Omega_{sx} = (2\pi)1$ MHz. (c,d) Resonance correction with ac Stark shifts. The parameters are the same as in panels (a) and (b) except for the frequency of the spin-locking drive $\omega = \omega_0 + \delta_z$ and the resonance condition $\omega_b = \omega_s + \omega - \Omega$ for the longitudinal signal, which cancels the ac Stark shift in the rotating frame.

Thus, to apply a larger bias amplitude for better sensitivity, one needs to extend the linear region by compensating the ac Stark shift by tuning to the corrected resonance condition $\omega = \omega_0 + \delta_z$, where $\delta_z = \delta_z(\omega)$ has a dependence on ω and the solution to ω, δ_z can be obtained numerically for a given Ω_b. We then simulate the same bias amplitude sweep with the corrected resonance conditions in Figs. 3(c) and 3(d) as a comparison to Figs. 3(a) and 3(b). The linear region now extends to a larger value of Ω_b for both longitudinal and

transverse signals, which demonstrates that a large bias amplitude, almost on the order of ω_s, improves the sensitivity. In principle, one can always use more orders of the perturbation expansion for better resonance corrections to expand the linear region further. However, when the value of Ω_b becomes even larger, the condition $\Omega_b \ll \tilde{\omega}_b = \omega_b - \omega$ is no longer satisfied, and our theory based on the perturbative Floquet approach starts to break down. Moreover, if the bias amplitude can approach the same order of magnitude as the signal frequency, preexisting protocols such as rotating-frame Rabi magnetometry without frequency mixing [15,68] can be utilized to perform the sensing task with better sensitivity.

In conclusion, although it is difficult to completely eliminate sensitivity degradation, this technique's sensitivity can approach that of the preexisting traditional sensing protocols without frequency mixing by increasing Ω_b.

VI. ARBITRARY-FREQUENCY VECTOR FIELD SENSING

Although the protocols described in Sec. IV are for sensing transverse and longitudinal signals separately, in this section we show that combining these protocols yields a method for sensing a vector ac field with an arbitrary-frequency range. By applying a single bias field with tunable frequency ω_b, the transverse and longitudinal components of a vector ac field can be separately measured under different resonance conditions through Rabi or CPMG methods. While MHz–GHz vector magnetometry has been extensively studied and demonstrated [14,68,73–80], our protocol paves the way to implement vector ac magnetometry in the high-frequency range (larger than a few GHz) and also serves as an alternative to existing protocols in the intermediate-frequency range (between 50 MHz and 2 GHz).

A. Principle

Consider a target signal that is a linearly polarized ac magnetic field that couples to a spin qubit in the lab frame as

$$H_s = [\Omega_{s\perp}(\cos\theta\sigma_x + \sin\theta\sigma_y) + \Omega_{sz}\sigma_z]\cos(\omega_s t). \tag{23}$$

We apply a circularly polarized bias field in the x-y plane with phase ϕ_b relative to the signal phase and calculate the effective Hamiltonian in the rotating frame following Eq. (6), which yields

$$\begin{aligned}\bar{H}_I = {} & \frac{\delta_z}{2}\sigma_z - \Omega_{T\perp}\cos(\omega_T t + \phi_b - \theta)\sigma_z \\ & + \Omega_{Tz}[\cos(\tilde{\omega}_T t + \phi_b)\sigma_x + \sin(\tilde{\omega}_T t + \phi_b)\sigma_y],\end{aligned} \tag{24}$$

where $\omega_T = \omega_b - \omega_s$ and $\tilde{\omega}_T = (\omega_b - \omega_0) - \omega_s$, the ac Stark shift is $\delta_z/2 = -(1/4)(\Omega_b^2/\tilde{\omega}_b + \Omega_{s\perp}^2/\omega_T - \Omega_{s\perp}^2/\tilde{\omega}_T)$, and the effective target signal amplitudes Ω_{Tz}, $\Omega_{T\perp}$ are given by Eqs. (14) and (20), respectively (with $\Omega_{s\perp}$ replacing Ω_{sx}). As quantum frequency mixing yields different frequencies and directions for the longitudinal and transverse components of the target signal, they can be independently detected under different resonance conditions. The sensing task is facilitated by applying a resonant control field $\Omega(t)$ such that the Hamiltonian in the rotating frame approximately reduces to

$$\begin{aligned}\bar{H}_I = {} & \frac{\Omega(t)}{2}\sigma_x - \Omega_{T\perp}\cos(\omega_T t + \phi_b - \theta)\sigma_z \\ & + \Omega_{Tz}\sin(\tilde{\omega}_T t + \phi_b)\sigma_y,\end{aligned} \tag{25}$$

as shown in Fig. 4(a). Here, we can safely neglect the ac Stark shifts and the effective term along x. The control field amplitude is set to implement either a continuous or pulsed sensing protocol [Fig. 4(b)].

Option 1: Rabi. We set the control field to be a continuous (static) field in the rotating frame, $\Omega(t) = \Omega$, and tune the bias frequency ω_b to sense the longitudinal and transverse components. When $\tilde{\omega}_T = \pm\Omega$, the longitudinal component [the σ_y term proportional to Ω_{sz} in Eq. (25)] is on resonance, and we can neglect the off-resonance transverse component. Then, Ω_{sz} can be obtained by measuring the rotating-frame Rabi oscillation of the initial spin-locked state $|+\rangle$ as shown in Eq. (16). To sense the transverse field $\Omega_{s\perp}$, we instead set $\omega_T = \pm\Omega$, so the corresponding frequency-mixed term [the σ_z term in Eq. (25)] is now on resonance and can similarly induce a rotating-frame Rabi oscillation.

In addition to measuring the amplitudes Ω_{sz} and $\Omega_{s\perp}$, Rabi oscillation can also reveal the transverse field direction θ by setting the initial state to $|0\rangle$ and controlling the bias field phase ϕ_b [68] (see Supplemental Material [81]). Under the resonance condition for the longitudinal component $\tilde{\omega}_T = \pm\Omega$, the Rabi signal is then $S(t) = (1/2) \times [1 \pm \sin(\Omega_{Tz}t)\sin(\phi_b)]$, which reveals the phase difference between signal and bias. With control over ϕ_b, the transverse direction θ can then be measured under the resonance condition for the transverse component $\omega_T = \pm\Omega$, yielding a Rabi signal $S(t) = (1/2)[1 \mp \sin(\Omega_{T\perp}t)\sin(\phi_b - \theta)]$. We note that similar methods of sensing the signal transverse direction have been demonstrated in vector ac magnetometry without frequency mixing [68].

Option 2: CPMG. Rather than applying a continuous drive, we modulate $\Omega(t)$ by periodically applying π pulses along the σ_x direction, with an interpulse delay τ. When we set the bias frequency so that $\tilde{\omega}_T = \pm\pi/\tau$, the σ_y term in Eq. (25) arising from the longitudinal field is on resonance with the CPMG sequence while we can neglect the transverse component. Measuring the population of the initial state $|+\rangle$ as a function of the pulse number yields $S(t) = (1/2)[1 + \cos(4\Omega_{Tz}t/\pi)]$, which allows extraction of the longitudinal amplitude Ω_{sz}. Performing the same

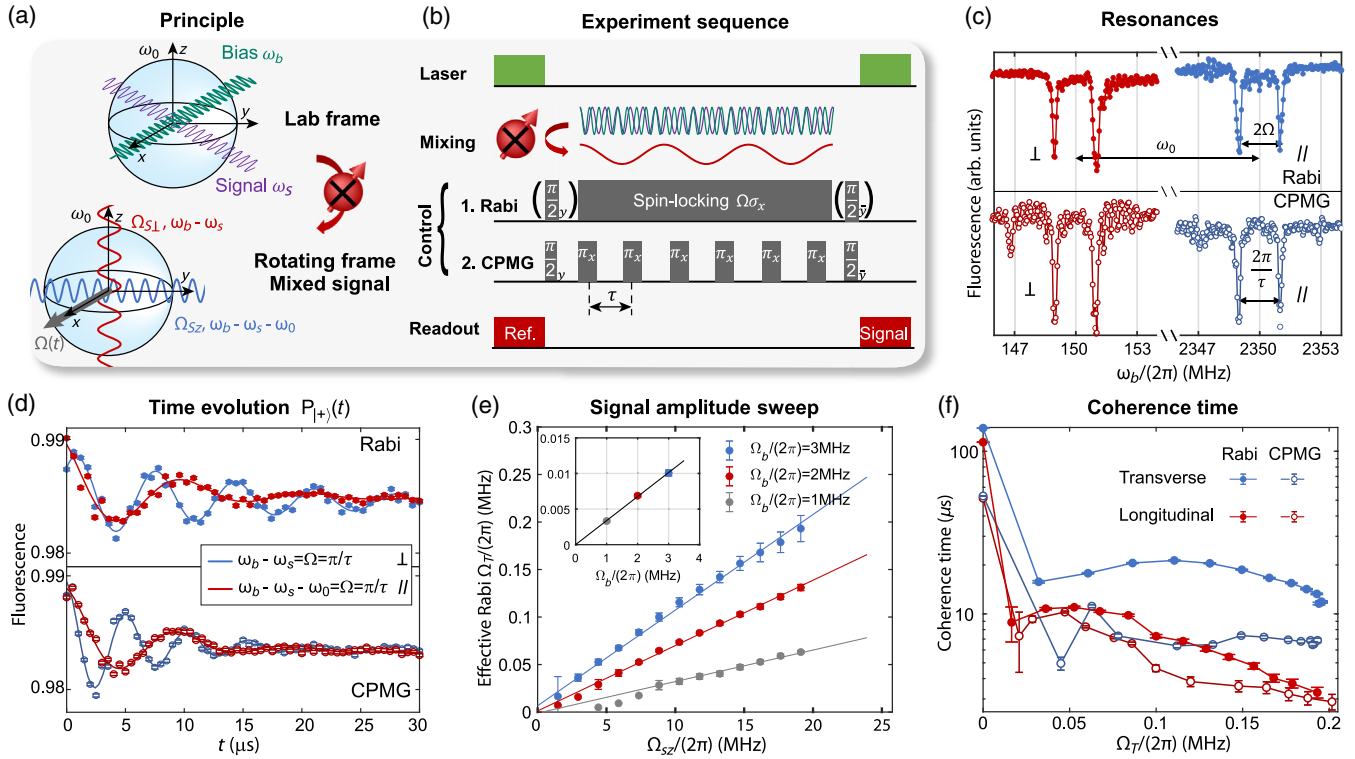

FIG. 4. Vector ac magnetometry. (a) Principle of vector ac magnetometry with quantum frequency mixing. (b) Experimental sequence. (c) ESR measurement. The initialization and readout state is $|+\rangle$. The control fields are set to $\Omega, \pi/\tau = (2\pi)1$ MHz, and the π pulse length for CPMG is 0.167 μs. A linearly polarized signal field with frequency $\omega_s = (2\pi)150$ MHz, phase $\phi_s = 0$, and amplitude $\Omega_{sx} = (2\pi)15.3$ MHz, $\Omega_{sz} = (2\pi)10.4$ MHz is applied as the target to be sensed. A bias field with tunable frequency ω_b is applied with amplitudes $\Omega_b = (2\pi)15.3$ MHz for the low-frequency range to sense the transverse signal and $\Omega_b = (2\pi)3$ MHz for the high-frequency range to sense the longitudinal signal. For the Rabi method, the evolution duration is set to 3.5 μs (4 μs) for the low- (high-) frequency range, while for the CPMG method, the pulse number is set to 6 (8) for the low- (high-) frequency range. (d) Time evolution measurement under resonance conditions. The experimental parameters are the same as in panel (c), and the data are fit to the function $S(t) = c_0 + 0.5c\cos(\Omega_T t)e^{-t/T_{2\rho\rho}} + \xi t$, where ξ is a phenomenological drift factor. (e) Signal amplitude sweep under different bias amplitudes. The Rabi frequency for the longitudinal component sensing is measured as a function of signal amplitude under three different bias field amplitudes. The slopes for the signal sweep under different bias amplitudes are plotted in the inset and fit to a linear trend. Because of large error bars (not shown) for ultraslow Rabi oscillation measurements, the first two (three) data points for $\Omega_b/(2\pi) = 2(1)$ MHz are not included when fitting the linear curve. (f) Measured coherence time $T_{2\rho\rho}$. The time evolution induced by the effective transverse and longitudinal signals is measured in the rotating frame. The signal amplitude is swept, while the other experimental parameters are the same as the time evolution measurement in panel (d).

experiment with $\omega_T = \pm\pi/\tau$ yields $S(t) = (1/2)[1 + \cos(4\Omega_{T\perp} t\cos(\theta)/\pi)]$, where we only retain the on-resonance transverse field in Eq. (25) and extract $\Omega_{s\perp}$. Note that we can further extract θ (and the signal phase ϕ_s, which is set to 0 here for simplicity) by controlling the bias field phase. For both cases, the measured signals depend on the relative phase ϕ_b and transverse direction of the target signal, θ, which can then be obtained with control over ϕ_b.

We note that many other sensing protocols could also be combined with quantum frequency mixing to broaden the range of accessible frequencies. For example, the Ramsey sequence [82] could be utilized to probe an ac signal through the ac Stark shift. A careful analysis of their performance requires not only the Floquet tools provided here but also a study of coherence times and other practical limitations that should be evaluated case by case.

B. Experimental demonstration

We use a NV ensemble in our home-built setup [70] to demonstrate arbitrary-frequency vector magnetometry. NV centers are solid-state defects in diamond with spin $S = 1$ that provide sensitive magnetometry using optically detected, magnetic resonance techniques. A static magnetic field $B_0 \approx 239$ G is applied along the NV axis to lift the degeneracy of the spin-1 ground states $|m_S = \pm 1\rangle$. The two ground states $|m_S = 0\rangle$ and $|m_S = -1\rangle$ are used as the logical $|0\rangle$ and $|1\rangle$ [83], with an energy gap of 2200 MHz. A 0.4-W green laser beam is focused to a spot of about 30 μm for polarization and fluorescence readout addressing about 10^{10} spins simultaneously. A 0.7-mm loop structure on a printed circuit board (PCB) delivers linearly polarized microwave (MW) and radio-frequency (rf) fields through

two input channels. Three synchronized channels of an arbitrary waveform generator (AWG) implement precise control over the MW and rf. Since all fields are applied by the same loop, we have Ω_{sy}, $\theta \equiv 0$.

We apply a vector ac signal with frequency $\omega_s = (2\pi)150$ MHz and a bias field with tunable frequency ω_b for quantum frequency mixing (protocols 1 and 3 in Table I). In Fig. 4(c), sweeping the bias frequency for both the Rabi and CPMG methods reveals resonances at $\omega_b = \omega_s \pm \Omega\,(\pi/\tau)$ and $\omega_b = \omega_s + \omega_0 \pm \Omega\,(\pi/\tau)$, corresponding to the transverse and longitudinal components of the signal field. Figure 4(d) shows the on-resonance time evolution for both components. We further experimentally confirm in Fig. 4(e) the linear dependence of the measured effective amplitudes, Ω_{Tz}, Ω_{Tx} [Eqs. (14) and (20)], on both the signal and bias amplitudes.

C. Performance: Decoherence and sensitivity

Although our setup is not optimized for high photon collection efficiency and noise suppression, we evaluate the performance of vector ac magnetometry using quantum frequency mixing by characterizing the sensitivity. We use the Rabi data in Fig. 4(d) to estimate the sensitivities η_z, η_x for the longitudinal and transverse components,

$$\eta_z = \frac{4\sigma_S\sqrt{t+t_d}}{c\epsilon_z\gamma_e t e^{-t/T_{2\rho\rho}}} \approx 7.2\frac{\mu\mathrm{T}}{\sqrt{\mathrm{Hz}}}, \tag{26}$$

$$\eta_x = \frac{2\sqrt{2}\sigma_S\sqrt{t+t_d}}{c\epsilon_x\gamma_e t e^{-t/T_{2\rho\rho}}} \approx 7.6\frac{\mu\mathrm{T}}{\sqrt{\mathrm{Hz}}}, \tag{27}$$

where for the calculation of η_z, η_x, $\sigma_S \approx 0.0094$, 0.0095, signal contrast $c \approx 0.01$, 0.008, and coherence time $T_{2\rho\rho} \approx 7.5$, 16.2 μs are obtained from the data fitting, and we have the sensitivity reduction factors $\epsilon_{z,x} \approx 0.01$, 0.016, and the sensing time and dead time $t, t_d = 10, 50$ μs for both cases.

The ultimate projection-noise limit of the sensitivity $\eta \propto 1/\sqrt{t}$ [13] is set by the coherence time of the signal-induced oscillation in the rotating frame, denoted by $T_{2\rho\rho}$ [70]. The upper limit of $T_{2\rho\rho}$ is given by the coherence time $T_{1\rho}$ of the state $|+\rangle$ in the absence of signal fields, which is the spin-locked state for Rabi sensing or the optimally protected state for CPMG. Theoretically, these coherence times are associated with the power spectral density (PSD) of stochastic magnetic fields due to various noise sources, and their quantitative relation has been extensively studied [21,68,70,84,85]. The coherence time of the rotating-frame Rabi oscillation can be written as

$$\frac{1}{T_{2\rho\rho}} \approx \frac{1}{4}\mathcal{S}_{\Omega_T}(0) + \frac{1}{8}\mathcal{S}_{\Omega}(\Omega_T) + \frac{3}{4}\mathcal{S}_z(\Omega) + \frac{5}{8}\mathcal{S}_x(\omega_0), \tag{28}$$

where $\mathcal{S}_j$ are the noise spectrum, with $j = x, z, \Omega, \Omega_T$ denoting the noise of the transverse and longitudinal spin bath fields, the spin-locking drive field, and the effective target signal field, respectively. In Fig. 4(f), we measure $T_{2\rho\rho}$ as a function of the state oscillation frequency by sweeping the signal amplitudes Ω_s. The nonmonotonic behavior was also observed in Ref. [70], which can be explained by the presence of two competing noise terms: $\mathcal{S}_{\Omega_T}(0)$, which increases as Ω_T, and $\mathcal{S}_{\Omega}(\Omega_T)$, which decreases as Ω_T. Here, we assume the noise is dominated by static and low-frequency components such as driving-field inhomogeneities. However, under ideal conditions when all control and bias fields are noiseless such that $\mathcal{S}_{\Omega_T} = \mathcal{S}_{\Omega} = 0$, and $\mathcal{S}_x(\omega_0) \sim 1/T_1$ is small, the dominant term is then only $\mathcal{S}_z(\Omega) \sim 1/T_{1\rho}$, which sets the limit of the coherence time to the spin-locking coherence $T_{1\rho}$. For the experimental measurement depicted in Fig. 4(f), the spin-locking coherence time approaches a timescale greater than 100 μs for the resonant driving amplitude $\Omega = (2\pi)1$ MHz (see a more complete discussion in Refs. [68,70]). Further optimizations [13], such as improving the photon collection efficiency [86], can improve the sensitivity and bring it closer to the best performances reported in other sensing protocols, with only a reduction factor $\epsilon_{x,z}$ difference.

The results in Fig. 4(f) show that the coherence time for sensing a transverse component is better than the longitudinal component and that the Rabi method provides longer coherence times than CPMG. Here, we briefly discuss possible reasons for this trend. Although dynamical decoupling—in particular, the pulsed CPMG protocol—can filter out static resonance shifts and inhomogeneities (mainly σ_z terms), the cancellation is better when the effective target signal Hamiltonian commutes with σ_z. In addition, the bias fields for transverse and longitudinal components are applied by rf and MW amplifiers with different electronics elements, which give rise to different noises. We note that similar results were also observed in the comparison of various concatenated continuous driving schemes, where the rotating-frame Rabi oscillations were induced by modulation fields [70], though the noise spectrum model there already provided reasonable explanations.

Further identification of various noise sources—as well as evaluation of the validity of different noise models in continuous, pulsed, and even mixed sensing protocols—will be of interest to achieve optimal protocols. In particular, since quantum frequency mixing down-converts a stochastic ac signal [term $\mathcal{S}_{\Omega_T}(0)$ in Eq. (28)] in the same way as a coherent signal, this paves the way to perform noise spectroscopy measurement with an arbitrary-frequency range.

VII. DISCUSSIONS AND CONCLUSIONS

In this work, we theoretically derive an intuitive but precise formula for calculating the time-dependent effective Hamiltonian in multimode Floquet problems, which is summarized as a quantum frequency mixing. Based on

the theoretical results, we propose the first quantum-sensing protocol with an arbitrary-frequency range, by converting target signal frequencies to the dynamic range of preexisting sensing protocols such as Rabi and CPMG. By combining frequency conversions for the transverse and longitudinal components of a target signal field, we propose the first arbitrary-frequency vector ac magnetometry. We then implement proof-of-principle experiments with a NV center ensemble in diamond to demonstrate vector magnetometry using both Rabi and CPMG methods and validate the theory in detail. We discuss the sensitivity of our setup and current limitations set by decoherence.

In practical applications, one potential limitation of our sensing protocol is the degradation of the sensitivity as the signal frequency increases. In addition to the method of increasing the bias field amplitude discussed in Sec. V, one can overcome such a limitation by properly choosing the polarization options for the bias field. For example, when the signal is transverse, choosing a longitudinal bias or a circularly polarized transverse bias [87] gives an improvement of the sensitivity by a factor of about ω_s/ω_0 in comparison to a linearly polarized transverse bias. To completely overcome such a degradation, one interesting direction of future research is to integrate our mixer and sensor with well-developed masers [42,43,88] to greatly enhance the sensitivity and frequency range of the quantum sensor simultaneously. Moreover, our protocol utilizes only one orientation of NV centers and can be implemented on single-NV setups [68], allowing for nanoscale spatial resolution. Thus, our work paves the way to build a quantum sensor with an arbitrary-frequency range, which is also capable of being combined with other state-of-the-art techniques to achieve high sensitivity [86,89], nanoscale resolution [90,91], arbitrary-frequency resolution [92–94], and k-space resolution [4].

Since the quantum frequency mixing protocols we developed are generally applicable to any Floquet systems, especially those under multiple driving frequencies, our work leads to broad applications beyond quantum sensing. In quantum control and quantum computation, multimode Floquet systems provide platforms for studying geometric phases and designing non-Abelian holonomic gates for noise-resilient quantum computation [69,95]. In a quantum simulation, the synthetic dimension of multimode Floquet systems has been utilized to engineer desired Hamiltonians [26] to study topological phases such as topological frequency conversion [46,47] and anomalous edge states [96]. In classical and quantum communications, quantum frequency mixing provides an alternative way to perform frequency modulation and frequency conversion [55–58] along with other operations in the same system, which is of interest for future study. Our theoretical calculations combine the advantage of the precise prediction of dynamics and physical insights, thus enriching the approaches targeting the aforementioned applications and opening up promising directions to develop more advanced protocols for quantum applications.

ACKNOWLEDGMENTS

This work was supported in part by the DARPA DRINQS program (Cooperative Agreement No. D18AC00024) and Q-Diamond Grant No. W911NF13D0001.

APPENDIX A: MULTIMODE FLOQUET THEORY

To derive a general framework to calculate the effective Hamiltonian due to frequency mixing, we start with a bimodal Floquet problem, which can be easily extended to any multimode Floquet problem. A time-dependent Hamiltonian with two frequency modes (ω_q, ω_r),

$$H(t) = \sum_{n=-\infty}^{\infty} \sum_{k=-\infty}^{\infty} H^{(n,k)} e^{in\omega_q t} e^{ik\omega_r t}, \tag{A1}$$

can be written in the Floquet space as a Floquet Hamiltonian

$$H_F = \sum_{n=-\infty}^{\infty} \sum_{k=-\infty}^{\infty} (H^{(n,k)} \otimes F_n^q \otimes F_k^r + \omega_q I \otimes F_z^q \otimes I + \omega_r I \otimes I \otimes F_z^r), \tag{A2}$$

where (n, k) is a pair of integer numbers denoting the Fourier expansion order, $F_n = \sum_m |m+n\rangle\langle m|$ is the ladder operator, and $F_z = \sum_n n|n\rangle\langle n|$ is the number operator. These operators satisfy the commutation relations $[F_z, F_n] = nF_n$, $[F_n, F_m] = 0$ and $F_n F_m = F_{n+m}$.

To find a solution in the form of a block-diagonalized Floquet matrix, we first separate out a diagonal part $H_F^{(0)}$ in the Floquet matrix and use a constant $\epsilon = 1$ to denote the order of magnitude, yielding

$$H_F^0 = \omega_q F_z^q + \omega_r F_z^r, \qquad H_F = H_F^{(0)} + \epsilon V, \tag{A3}$$

where the tensor product signs are eliminated for simplicity. Then, we transform to a different frame using a unitary transformation $U = e^S$, with S anti-Hermitian, to find an effective Hamiltonian

$$\tilde{H}_F = e^S H_F e^{-S} = H_F + [S, H_F] + \frac{1}{2}[S, [S, H_F]] + \ldots, \tag{A4}$$

which can be made approximately block diagonal by eliminating the lowest-order, off-diagonal terms. We thus expand S and the transformed Hamiltonian to different orders of ϵ, $S = \sum_k \epsilon^k S_k$ and $\tilde{H}_F = \sum_k \epsilon^k \tilde{H}_k$, yielding

$$\tilde{H}_F = H_F^{(0)} + \epsilon(V + [S_1, H_F^{(0)}]) + \epsilon^2\left([S_2, H_F^{(0)}] + [S_1, V] + \frac{1}{2}[S_1, [S_1, H_F^{(0)}]]\right) + \ldots. \tag{A5}$$

For simplicity, we assume that V is time dependent in the Hilbert space and contains no terms commuting with the diagonal part of the Floquet matrix. Then, V introduces an off-diagonal term to first order, and to cancel it out, we set

$$V + \left[S_1, H_F^{(0)}\right] = 0, \qquad S_1 = -\Gamma^{-1}(V). \tag{A6}$$

Here, $\Gamma(X) = [X, H_F^{(0)}]$ and $\Gamma^{-1}(X) = -\sum_{k\neq h} P_k X P_h/(E_0^k - E_0^h)$ is its inverse [97], where P_k is the projection operator of the diagonal Floquet Hamiltonian, such that $H_F^{(0)} = \sum_k P_k E_0^k$. Using the relations

$$\Gamma^{-1}(F_n^q F_k^r) = -\frac{1}{n\omega_q + k\omega_r} F_n^q F_k^r, \;\; \Gamma^{-1}(F_{n_0}^q F_{k_0}^r) = 0, \tag{A7}$$

and $V = \sum_{n,k} H^{(n,k)} F_n^q F_k^r$, we obtain an explicit expression for S_1:

$$S_1 = \sum_{(n,k)\neq(n_0,k_0)} \frac{H^{(n,k)}}{n\omega_q + k\omega_r} F_n^q F_k^r, \tag{A8}$$

where the pairs (n_0, k_0) satisfy $n_0\omega_q + k_0\omega_r = 0$; that is, they denote the resonance condition. We now have the relation

$$[S_1, V] + \frac{1}{2}\left[S_1, \left[S_1, H_F^{(0)}\right]\right] = \frac{1}{2}[S_1, V].$$

Then, the second-order correction is

$$\tilde{H}_F^{(2)} = \left[S_2, H_F^{(0)}\right] + \frac{1}{2}[S_1, V] = \left[S_2, H_F^{(0)}\right] - \frac{1}{2}\sum_{m,h}\sum_{(n,k)\neq(n_0,k_0)} \frac{[H^{(m-n,h-k)}, H^{(n,k)}]}{n\omega_q + k\omega_r} F_m^q F_h^r. \tag{A9}$$

In Ref. [52], a projection operator simply eliminates $[S_2, H_F^{(0)}]$, but there, the summation was restricted to on-resonance terms only, $(m, h) = (n_0, k_0)$. Here, we follow a slightly different route, where the second term in Eq. (A9) is the same expression as $\Lambda_F^{(2)}$ in Ref. [52] but with the sum not restricted to n_0, k_0. We can now divide this term into two parts such that

$$\tilde{H}_F^{(2)} = \left[S_2, H_F^{(0)}\right] + W + \bar{H}_F^{(2)}, \tag{A10}$$

where

$$W = -\frac{1}{2}\sum_{m,h\notin\langle m,h\rangle}\sum_{(n,k)\neq(n_0,k_0)} \frac{[H^{(m-n,h-k),H^{(n,k)}}]}{n\omega_q + k\omega_r} F_m F_h, \tag{A11}$$

$$\bar{H}_F^{(2)} = -\frac{1}{2}\sum_{\langle m,h\rangle}\sum_{(n,k)\neq(n_0,k_0)} \frac{[H^{(m-n,h-k),H^{(n,k)}}]}{n\omega_q + k\omega_r} F_m^q F_h^r, \tag{A12}$$

where the summation for $\bar{H}_F^{(2)}$ is restricted to the indices $\langle m, h\rangle$ labeling only the non-negligible terms (e.g., zero frequency, on resonance, and low frequencies that are picked up by the sensing protocol), and W is the complementary term. We can now use S_2 to cancel out W, by setting

$$[S_2, H_F^{(0)}] + W = 0. \tag{A13}$$

If we keep all terms in Eq. (A9) (and neglect their effects later, e.g., with RWA, resonance, etc.), we can set $W = 0$, which also implies $S_2 = 0$. So with either strategy, the relevant second-order correction is

$$\tilde{H}_F^{(2)} = -\frac{1}{2}\sum_{\langle m,h\rangle}\sum_{(n,k)\neq(n_0,k_0)} \frac{[H^{(n,k)}, H^{(m-n,h-k)}]}{n\omega_r + k\omega_q} F_m^q F_h^r. \tag{A14}$$

The effective Hamiltonian in Hilbert space is now

$$\begin{aligned}\bar{H}(t) &= \sum_{n',k'}\langle n, k|H_F^{(0)} + H_F^{(1)} + H_F^{(2)} + \cdots|n+n', k+k'\rangle \\ &= \sum_{\langle m,h\rangle}[H^{(m,h)} + H_{(2)}^{(m,h)} + \cdots]e^{i(m\omega_q + h\omega_r)t},\end{aligned} \tag{A15}$$

where the second- and third-order terms are [98]

$$H_{(2)}^{(m,h)} = -\frac{1}{2}\sum_{n,k}\frac{[H^{(m-n,h-k)}, H^{(n,k)}]}{n\omega_q + k\omega_r}, \tag{A16}$$

$$H_{(3)}^{(m,h)} = \frac{1}{2}\sum_{n,k,n',k'}\frac{[[H^{(n,k)}, H^{(m-n-n'),(h-k-k')}], H^{(n',k')}]}{(n\omega_q + k\omega_r)^2} + \frac{1}{3}\sum_{n,k,n'',k''}\frac{[[H^{(n,k)}, H^{(m-n-n'',h-k-k'')}], H^{(n'',k'')}]}{(n\omega_q + k\omega_r)(n''\omega_q + k''\omega_r)}. \tag{A17}$$

While the range of values $\langle m, h\rangle$ is flexible in different applications [50–52], in this work we focus on slowly varying terms with a near-resonance condition $m\omega_q + h\omega_r \approx 0$ or $m\omega_q + h\omega_r \ll \omega_l$, where $\omega_l \in \{n\omega_q + k\omega_r | n, k \in \mathbb{Z}, n\omega_q + k\omega_r \neq 0, H^{(n,k)} \neq 0\}$, to describe frequency mixing due to different frequency modes, as we neglect terms oscillating at high frequency, which rapidly average out.

The theoretical calculations up to second order are summarized as a simple correspondence in Eq. (6) in the main text. These results can also give rise to time-independent effective Hamiltonians as discussed in Refs. [50–52]. Here, we show an example of calculating an ac Stark shift with Eq. (6) for time-independent cases. For a qubit with an energy gap ω_0 under a circularly polarized driving field $(\Omega/2)[\cos(\omega t)\sigma_x + \sin(\omega t)\sigma_y]$ with detuning $\delta = \omega - \omega_0$, the effective Hamiltonian can be calculated in the rotating frame, where the unmixed Hamiltonian is $(\Omega/2)[\cos(\delta t)\sigma_x + \sin(\delta t)\sigma_y]$, yielding $H_1 = (\Omega/2)\sigma^-$, $H_2 = (\Omega/2)\sigma^+$, and $\omega_1 = -\omega_2 = \delta$. The effective Hamiltonian is then calculated as $-[\Omega^2/(4\delta)]\sigma_z$, which is exactly the ac Stark shift induced by a detuned oscillating field. This result is consistent with the calculation in standard textbooks on atomic physics [99].

APPENDIX B: QUANTUM FREQUENCY MIXING

1. Longitudinal signals

a. Case 1: Linearly polarized bias and signal (lab-frame analysis of Protocol 1 in Table I)

In the main text, for both the effective transverse and longitudinal signals, Rabi oscillations in the rotating frame are used to extract the signal amplitudes. Here, we show that an effective mixed signal in the x-y plane transformed from a longitudinal unmixed signal can induce Rabi oscillations in the lab frame. We start with the calculation of the effective Hamiltonian in the lab frame; then, we note that a more precise calculation should be performed in the rotating frame, which will be discussed shortly.

If both the bias field with amplitude Ω_b and signal with amplitude Ω_{sz} are linearly polarized, the Hamiltonian in the lab frame is

$$H = \frac{\omega_0}{2}\sigma_z + \Omega_b \cos(\omega_b t + \phi_b)\sigma_x + \Omega_{sz}\cos(\omega_s t + \phi_s)\sigma_z. \tag{B1}$$

This is a bimodal Floquet problem with two frequency modes (ω_b, ω_s). The nonzero Fourier components of the Hamiltonian H in Eq. (B1) are $H^{(0,0)} = (\omega_0/2)\sigma_z$, $H^{(\pm 1,0)} = (\Omega_b e^{\pm i\phi_b}/2)\sigma_x$, and $H^{(0,\pm 1)} = (\Omega_{sz}e^{\pm i\phi_s}/2)\sigma_z$. We assume $\Omega_b, \Omega_{sz}, |\omega_s - \omega_b| \ll \omega_{s,b}$ and consider the following frequencies that satisfy the near-resonance condition $m\omega_b + h\omega_s \approx 0$: (1) $(m,h) = (0,0)$ such that $m\omega_b + h\omega_s = 0$, giving rise to the ac Stark shift; (2) $(m,h) = (\pm 1, \mp 1)$ such that $m\omega_b + h\omega_s = \pm(\omega_b - \omega_s)$, giving rise to the frequency-mixed Rabi drive (target signal). For each case, we use Eq. (A16) to calculate the second-order effective Hamiltonian term, where the values of (n,k) in the summation go through all integer numbers satisfying $n\omega_b + k\omega_s \neq 0$. For example, for $(m,h) = (+1,-1)$, the values of (n,k) resulting in nonvanishing second-order terms in Eq. (A16) are $(n,k) = (0,-1)$ and $(n,k) = (+1,0)$; thus, the second-order term can be calculated as

$$\frac{1}{2}\left(\frac{1}{\omega_b} + \frac{1}{\omega_s}\right)[H^{(+1,0)}, H^{(0,-1)}]e^{i(\omega_b - \omega_s)t},$$

which again validates the formula in Eq. (6) in the main text. To calculate the complete effective Hamiltonian in the lab frame, we sum up all the frequency-mixed terms and obtain

$$\begin{aligned}\bar{H} &= \frac{\omega_0}{2}\sigma_z + \frac{1}{\omega_b}[H^{(1,0)}, H^{(-1,0)}] + \frac{1}{\omega_s}[H^{(0,1)}, H^{(0,-1)}] \\ &\quad + \left[\frac{1}{2}\left(\frac{1}{\omega_b} + \frac{1}{\omega_s}\right)[H^{(1,0)}, H^{(0,-1)}]e^{i(\omega_b - \omega_s)t} + \text{H.c.}\right] \\ &= \frac{\omega_0}{2}\sigma_z + \Omega_{Tz}\sin[(\omega_b - \omega_s)t + (\phi_b - \phi_s)]\sigma_y,\end{aligned} \tag{B2}$$

where the target signal amplitude is

$$\Omega_{Tz} = \frac{\Omega_b \Omega_{sz}}{2}\left(\frac{1}{\omega_b} + \frac{1}{\omega_s}\right). \tag{B3}$$

When $|\omega_b - \omega_s| = \omega_0$, a resonance condition is satisfied and a Rabi oscillation signal $S(t)$ is obtained when monitoring the population of an initial state $|0\rangle$ in the lab frame such that

$$S(t) = P_{|0\rangle}(t) = \frac{1}{2}[1 + \cos(\Omega_{Tz}t)]. \tag{B4}$$

The ac Stark shift of the linearly polarized bias field is not predicted from the lab-frame calculation, keeping terms up to second-order expansion in the perturbation. A more precise calculation of the effective Hamiltonian should be performed in the rotating frame.

b. Case 2: Linearly polarized bias and signal (rotating-frame analysis of Protocol 1 in Table I)

Here, we analyze case 1 again but in a rotating frame defined by $U = e^{-i(\omega_0 t/2)\sigma_z}$. This transforms the Hamiltonian in Eq. (B1) to

$$\begin{aligned}H_I &= \Omega_{sz}\cos(\omega_s t + \phi_s)\sigma_z \\ &\quad + \frac{\Omega_b}{2}[\cos(\tilde{\omega}_b t + \phi_b)\sigma_x + \sin(\tilde{\omega}_b t + \phi_b)\sigma_y] \\ &\quad + \frac{\Omega_b}{2}[\cos(\tilde{\tilde{\omega}}_b t + \phi_b)\sigma_x - \sin(\tilde{\tilde{\omega}}_b t + \phi_b)\sigma_y],\end{aligned} \tag{B5}$$

where $\tilde{\omega}_b = \omega_b - \omega_0$ and $\tilde{\tilde{\omega}}_b = \omega_b + \omega_0$ are the shifted bias frequencies. The rotating-frame Hamiltonian H_I describes a three-mode Floquet problem. We assume $\Omega_b, \Omega_{sz}, |\omega_b - \omega_0 \pm \omega_s| \ll \omega_s, \tilde{\omega}_b, \tilde{\tilde{\omega}}_b$ and neglect other fast oscillating frequencies such as $\omega_b + \omega_0 \pm \omega_s$; then, we obtain the effective Hamiltonian in the rotating frame,

$$\bar{H}_I = \frac{\delta_z}{2}\sigma_z + \Omega_{Tz}[\cos[(\omega_b - \omega_0 - \omega_s)t + (\phi_b - \phi_s)]\sigma_x + \sin[(\omega_b - \omega_0 - \omega_s)t + (\phi_b - \phi_s)]\sigma_y] - \Omega'_{Tz}[\cos[(\omega_b - \omega_0 + \omega_s)t + (\phi_b + \phi_s)]\sigma_x + \sin[(\omega_b - \omega_0 + \omega_s)t + (\phi_b + \phi_s)]\sigma_y]. \quad \text{(B6)}$$

The ac Stark shift term is

$$\frac{\delta_z}{2} = -\frac{\Omega_b^2\omega_0}{2(\omega_b^2 - \omega_0^2)}, \quad \text{(B7)}$$

and the target signal amplitudes are

$$\Omega_{Tz} = \frac{\Omega_b\Omega_{sz}}{4}\left(\frac{1}{\omega_b - \omega_0} + \frac{1}{\omega_s}\right), \quad \text{(B8)}$$

$$\Omega'_{Tz} = \frac{\Omega_b\Omega_{sz}}{4}\left(\frac{1}{\omega_0 - \omega_b} + \frac{1}{\omega_s}\right). \quad \text{(B9)}$$

We note that at most one of the two conditions $\omega_b - \omega_0 \pm \omega_s \ll \omega_s$ can be satisfied in practical experimental conditions. In the main text, the term with amplitude Ω'_{Tz} is neglected; here, we include both Ω_{Tz} and Ω'_{Tz} terms for completeness, as resonance conditions can be used with the protocols outlined in Table I.

If we apply a linearly polarized spin-locking drive $\Omega\cos(\omega_0 t)\sigma_x$ to create a static field $\Omega \gg \delta_z, \Omega_{Tz}$ along the x axis in the rotating frame, then the Hamiltonian can be simplified further to

$$\bar{H}_I = \frac{\Omega}{2}\sigma_x + \Omega_{Tz}\sin[(\omega_b - \omega_0 - \omega_s)t + (\phi_b - \phi_s)]\sigma_y - \Omega'_{Tz}\sin[(\omega_b - \omega_0 + \omega_s)t + (\phi_b + \phi_s)]\sigma_y, \quad \text{(B10)}$$

where the total ac Stark shift $[\delta_z/2 + \Omega^2/(8\omega_0)]\sigma_z$ is neglected. Here, $\Omega^2/(8\omega_0)$ is the Bloch-Siegert shift due to the counterrotating term of the spin-locking drive.

When the resonance condition $|\omega_b - \omega_0 - \omega_s| = \Omega$ (or $|\omega_b - \omega_0 + \omega_s| = \Omega$) is satisfied, a Rabi oscillation signal $S(t)$ is obtained when monitoring the population of the initial state $|+\rangle = (|0\rangle + |1\rangle)/\sqrt{2}$ in the rotating frame such that

$$S(t) = P_{|+\rangle}(t) = \frac{1}{2}[1 + \cos(\Omega_{Tz}t)]. \quad \text{(B11)}$$

For both ultrahigh signal frequencies $\Omega \ll \omega_0 < \omega_s$ and intermediate signal frequencies $\Omega \ll \omega_s < \omega_0$, the effective Rabi frequency is reduced to $\Omega_b\Omega_{sz}/2\omega_s$, leading to a sensitivity reduction factor $\epsilon_z = \Omega_b/2\omega_s$.

We note that the derivation here can also be used to describe the lab-frame Rabi in case 1 by setting $\Omega = 0$. However, the effective Rabi frequency and ac Stark shift obtained in the rotating frame are different from those in the lab frame with the same order-of-perturbation calculation. In Appendix B 1 d, we discuss their comparison in detail and show that the rotating-frame calculation is more precise.

c. Case 3: Circularly polarized bias and linearly polarized signal (Protocol 2 in Table I)

When the bias field is circularly polarized and the signal field is linearly polarized, the Hamiltonian in the rotating frame is

$$H_I = \Omega_{sz}\cos(\omega_s t + \phi_s)\sigma_z + \frac{\Omega_b}{2}[\cos(\tilde{\omega}_b t + \phi_b)\sigma_x + \sin(\tilde{\omega}_b t + \phi_b)\sigma_y]. \quad \text{(B12)}$$

By solving this bimodal Floquet problem, we obtain the effective Hamiltonian in the same form as Eq. (B6) with the same target signal amplitudes and a slightly different ac Stark shift term,

$$\frac{\delta_z}{2} = -\frac{\Omega_b^2}{4(\omega_b - \omega_0)}. \quad \text{(B13)}$$

Under the same resonance conditions, the rotating-frame Rabi oscillations of an initial spin-locked state can be induced by the effective target signal with the same form as Eq. (B11).

d. Comparison of lab-frame and rotating-frame calculations

We notice that case 1 is a special case of case 2 when $\Omega = 0$; however, the obtained ac Stark shift and target signal amplitude are different. Under the resonance condition $\omega_b = \omega_s + \omega_0$, the lab-frame derivation gives the effective Rabi frequency $(\Omega_b\Omega_{sz}/2)[1/\omega_s + 1/(\omega_s + \omega_0)]$, whereas the rotating-frame derivation gives the effective Rabi frequency $\sqrt{(\Omega_b\Omega_{sz}/\omega_s)^2 + \delta_z^2}$, which takes the ac Stark shift into account. For an ultrahigh signal frequency, $\omega_s \gg \omega_0$, the two results are approximately the same, but for an intermediate frequency, $\omega_s < \omega_0$, the two results are quite different since the ac Stark shift is non-negligible. In Fig. 5, we simulate the Fourier spectrum of the lab-frame Rabi oscillations as a function of the signal frequency and compare this with the theoretical predictions, which validates that the Floquet predictions in the rotating frame are more precise.

We further study this comparison by evaluating the effective Hamiltonian in the lab frame up to third order [50,51], which gives an ac Stark shift term $\delta_z/2 \sim -\Omega_b^2\omega_0/(2\omega_b^2)$ due to the mixing of three frequencies

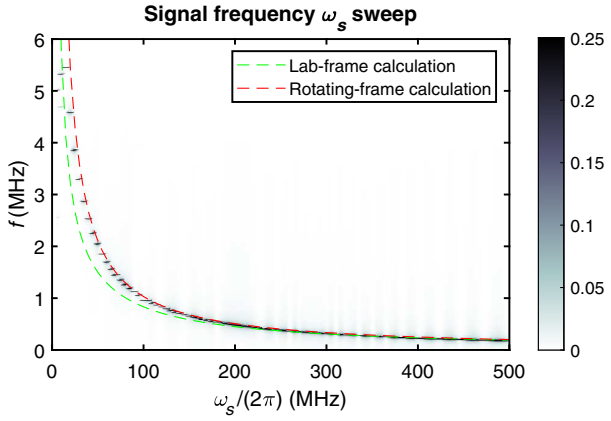

FIG. 5. Signal frequency ω_s sweep simulation. The population on initial state $|0\rangle$ is measured as $P_{|0\rangle}(t)$, and the intensity plot is the Fourier spectrum of $P_{|0\rangle}(t)$. Both the signal (along z) and bias field are linearly polarized with $\phi_b, \phi_s = \pi/2, 0$ and $\Omega_b = \Omega_{sz} = (2\pi)10$ MHz. The resonance condition $\omega_b = \omega_s + \omega_0$ with $\omega_0 = (2\pi)50$ MHz is satisfied. The calculation in the lab frame is given by Eq. (B3), and the one in the rotating frame is given by Eq. (B8) with the ac Stark shift taken into account (see Supplemental Material for more details).

$\omega_b, -\omega_b, 0$, which is still different from the one given by the rotating-frame analysis $\delta_z/2 \approx -\Omega_b^2\omega_0/(2(\omega_b^2 - \omega_0^2))$ but is already closer. When $\omega_b \gg \omega_0$, the two results become similar again. This comparison can be explained by examining the orders of magnitude of the effective Hamiltonian terms in Eq. (A15). In the lab frame, a large static term $(\omega_0/2)\sigma_z$ enters the numerator in the perturbation calculation, and the calculation of mixed terms is precise only for $\omega_s \gg \omega_0$. However, this large static term is canceled by the transformation to the rotating frame, and the perturbation analysis is precise as long as $\Omega_b, \Omega_{sz} \ll \omega_b - \omega_0, \omega_s$.

We note that a similar argument of the calculation accuracy should also apply to the Jacobi-Anger method [69]. To obtain a more precise result, the reference frame for the theoretical analysis should be carefully selected.

2. Transverse signals

a. Case 1: Linearly polarized bias and signal (Protocol 3 in Table I)

When both the bias and signal fields are transverse and linearly polarized, the Hamiltonian in the lab frame is

$$H = \frac{\omega_0}{2}\sigma_z + \Omega_b \cos(\omega_b t + \phi_b)\sigma_x + \Omega_{sx}\cos(\omega_s t + \phi_s)\sigma_x. \tag{B14}$$

In the rotating frame defined by $U = e^{-i(\omega_0 t/2)\sigma_z}$, we obtain

$$\begin{aligned} H_I = {} & \frac{\Omega_b}{2}[\cos(\tilde{\omega}_b t + \phi_b)\sigma_x + \sin(\tilde{\omega}_b t + \phi_b)\sigma_y] \\ & + \frac{\Omega_b}{2}[\cos(\tilde{\tilde{\omega}}_b t + \phi_b)\sigma_x - \sin(\tilde{\tilde{\omega}}_b t + \phi_b)\sigma_y] \\ & + \frac{\Omega_{sx}}{2}[\cos(\tilde{\omega}_s t + \phi_s)\sigma_x + \sin(\tilde{\omega}_s t + \phi_s)\sigma_y] \\ & + \frac{\Omega_{sx}}{2}[\cos(\tilde{\tilde{\omega}}_s t + \phi_s)\sigma_x - \sin(\tilde{\tilde{\omega}}_s t + \phi_s)\sigma_y], \end{aligned} \tag{B15}$$

where $\tilde{\tilde{\omega}}_{b,s} = \omega_{b,s} + \omega_0$, $\tilde{\omega}_{b,s} = \omega_{b,s} - \omega_0$.

The Hamiltonian in Eq. (B15) is a four-mode Floquet problem. Assuming that $\Omega_b, \Omega_{sx}, |\omega_b - \omega_s| \ll \tilde{\omega}_{s,b}, \tilde{\tilde{\omega}}_{s,b}$ and neglecting fast oscillating terms, we obtain the effective Hamiltonian

$$\bar{H}_I = \frac{\delta_z}{2}\sigma_z - \Omega_{Tx}\cos[(\omega_b - \omega_s)t + (\phi_b - \phi_s)]\sigma_z, \tag{B16}$$

where the ac Stark shift is

$$\frac{\delta_z}{2} = -\frac{\Omega_b^2\omega_0}{2(\omega_b^2 - \omega_0^2)} - \frac{\Omega_{sx}^2\omega_0}{2(\omega_s^2 - \omega_0^2)}, \tag{B17}$$

and the target signal amplitude is

$$\Omega_{Tx} = \frac{\Omega_b\Omega_{sx}}{2}\left(\frac{\omega_0}{\omega_b^2 - \omega_0^2} + \frac{\omega_0}{\omega_s^2 - \omega_0^2}\right). \tag{B18}$$

If we apply a linearly polarized spin-locking drive to create a static field Ω along x in the rotating frame, the Hamiltonian is then approximately simplified to

$$\bar{H}_I = \frac{\Omega}{2}\sigma_x - \Omega_{Tx}\cos[(\omega_b - \omega_s)t + (\phi_b - \phi_s)]\sigma_z, \tag{B19}$$

where the total ac Stark shift $[\delta_z/2 + \Omega^2/(8\omega_0)] \ll \Omega$ is neglected.

When $|\omega_b - \omega_s| = \Omega$, the resonance condition is satisfied, and a Rabi oscillation signal $S(t)$ is obtained by monitoring the population of the initial state $|+\rangle$ in the rotating frame such that

$$S(t) = P_{|+\rangle}(t) = \frac{1}{2}[1 + \cos(\Omega_{Tx}t)]. \tag{B20}$$

For an ultrahigh signal frequency $\omega_{b,s} \gg \omega_0 \gg \Omega$, the effective Rabi frequency is reduced to $\Omega_b\Omega_{sx}\omega_0/\omega_s^2$, yielding a sensitivity reduction factor $\epsilon_x = \Omega_b\omega_0/\omega_s^2$. For an intermediate signal frequency $\Omega \ll \omega_{b,s} \ll \omega_0$, the effective Rabi frequency is reduced to $\Omega_b\Omega_{sx}/\omega_0$, and the sensitivity reduction factor is $\epsilon_x = \Omega_b/\omega_0$.

b. Case 2: Circularly polarized bias and signal

When both the bias and signal fields are transverse and circularly polarized, the Hamiltonian in the rotating frame is

$$H_I = \frac{\Omega_b}{2}[\cos(\tilde{\omega}_b t + \phi_b)\sigma_x + \sin(\tilde{\omega}_b t + \phi_b)\sigma_y] + \frac{\Omega_{sx}}{2}[\cos(\tilde{\omega}_s t + \phi_s)\sigma_x + \sin(\tilde{\omega}_s t + \phi_s)\sigma_y]. \quad \text{(B21)}$$

By solving the bimodal Floquet problem in Eq. (B21), we obtain the effective Hamiltonian in the same form as Eq. (B16) with the ac Stark shift term

$$\frac{\delta_z}{2} = -\frac{\Omega_b^2}{4(\omega_b - \omega_0)} - \frac{\Omega_{sx}^2}{4(\omega_s - \omega_0)} \quad \text{(B22)}$$

and the target signal amplitude

$$\Omega_{Tx} = \frac{\Omega_b \Omega_{sx}}{4}\left(\frac{1}{\omega_b - \omega_0} + \frac{1}{\omega_s - \omega_0}\right). \quad \text{(B23)}$$

The rotating-frame Rabi oscillations also have the same signal form as Eq. (B20) under the same resonance condition $|\omega_b - \omega_s| = \Omega$.

For an ultrahigh signal frequency $\omega_{b,s} \gg \omega_0 \gg \Omega$, the effective Rabi frequency is reduced to $\Omega_b\Omega_{sx}/2\omega_s$; thus, the sensitivity reduction factor is $\epsilon_x = \Omega_b/(2\omega_s)$. For an intermediate signal frequency $\Omega \ll \omega_{b,s} \ll \omega_0$, the effective Rabi frequency is reduced to $\Omega_b\Omega_{sx}/(2\omega_0)$, and the sensitivity reduction factor is $\epsilon_x = \Omega_b/(2\omega_0)$.

c. Case 3: Circularly polarized bias and linearly polarized signal (Protocol 4 in Table I)

Comparing the previous cases 1 and 2 shows that the sensitivity for linearly polarized bias and signal fields (case 1) is degraded by an additional factor ω_0/ω_s in comparison to case 2 (both fields are circularly polarized). Unfortunately, we do not expect most signals to be circularly polarized (hence, we did not include case 2 in Table I). Still, here we show that even with a linearly polarized signal field, we can eliminate such an additional sensitivity reduction by applying a circularly polarized bias source.

The Hamiltonian in the rotating frame is now

$$H_I = \frac{\Omega_b}{2}[\cos(\tilde{\omega}_b t + \phi_b)\sigma_x + \sin(\tilde{\omega}_b t + \phi_b)\sigma_y] + \frac{\Omega_{sx}}{2}[\cos(\tilde{\omega}_s t + \phi_s)\sigma_x + \sin(\tilde{\omega}_s t + \phi_s)\sigma_y] + \frac{\Omega_{sx}}{2}[\cos(\tilde{\tilde{\omega}}_s t + \phi_s)\sigma_x - \sin(\tilde{\tilde{\omega}}_s t + \phi_s)\sigma_y]. \quad \text{(B24)}$$

By solving the three-mode Floquet problem in Eq. (B24), we obtain the effective Hamiltonian in the same form as Eq. (B16) with the same target signal amplitude and a slightly different ac Stark shift term

$$\frac{\delta_z}{2} = -\frac{\Omega_b^2}{4(\omega_b - \omega_0)} - \frac{\Omega_{sx}^2\omega_0}{2(\omega_s^2 - \omega_0^2)}. \quad \text{(B25)}$$

The rotating-frame Rabi magnetometry signal has the same form as Eq. (B20) under the same resonance condition $|\omega_b - \omega_s| = \Omega$. The target signal amplitude and the sensitivity are thus similar to case 2, which has a smaller degradation factor than case 1.

3. Additional strategies to improve the sensitivity

Under a large bias field Ω_b and spin-locking control amplitude Ω, higher-order terms from perturbation theory become important, as additional frequency modes are no longer negligible. These terms might potentially limit the optimal sensitivity. In addition, the possible frequency mixing involving the control fields $\Omega(t)$ might also induce imperfections.

As we mentioned, some of the higher-order terms could be corrected for, by adjusting the working protocols. When correcting the ac Stark shift by adjusting the resonance condition of the control field Ω to $\omega = \omega_0 + \delta_z(\omega)$ (Sec. V), a detuning term in the rotating frame $-\delta_z\sigma_z/2$ could give rise to additional mixed Hamiltonian terms. Since the simulation matches the theoretical predictions when the bias and signal amplitudes are not too large, as shown in both Figs. 3 and 5, these imperfections only become important when the bias or control amplitudes become large compared to mode frequencies.

Another way to suppress the ac Stark shift to improve the sensitivity is to increase the resonant driving amplitude Ω. In the Supplemental Material [81], we simulate the dependence of the bias amplitude Ω_b under different drive amplitudes Ω, which show that the deviation from the linearity appears at a larger Ω_b under a larger Ω. Thus, correcting the ac Stark shift and increasing Ω may yield a higher sensitivity to vector ac fields.

APPENDIX C: SIMULATION VALIDATION

In the main text and Appendix B, we validate the theoretical predictions of the various quantum frequency mixing protocols by simulating a few exemplary cases. In this section, we add more detailed simulations for all six cases discussed in Appendix B to further validate our theoretical results.

1. Phase dependence

As introduced in the main text, the relative phase between the bias field and the signal field is used to extract the transverse signal direction; thus, it is important to validate the phase dependence of the effective Hamiltonian. Since the population measurement on the initial state $|+\rangle = (|0\rangle + |1\rangle)/\sqrt{2}$ does not reveal the phase information $\phi_b - \phi_s$ in the effective Hamiltonian [Eqs. (B2), (B10), and (B16)], here we instead monitor the population of the initial state $|0\rangle$ (for the sensing protocol in the lab frame, i.e., case 1 of longitudinal signal sensing, we monitor $|+\rangle$ in the lab frame). Before we move forward to the simulation validation of the phase dependence, we first provide an

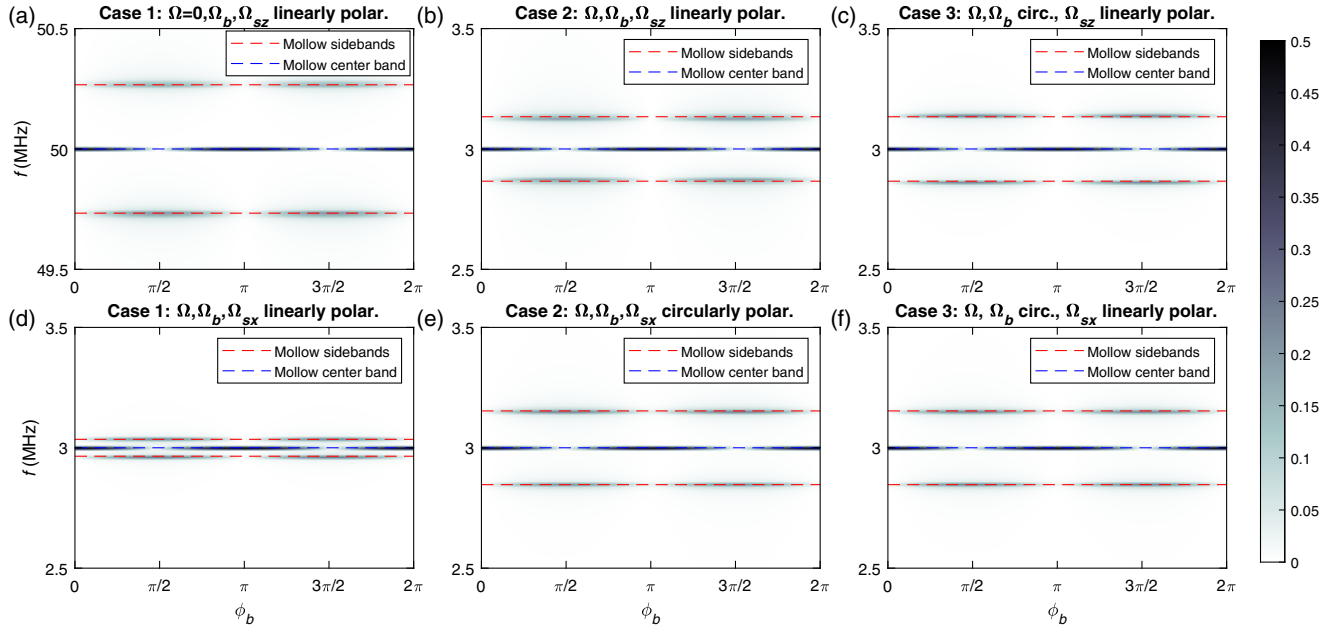

FIG. 6. Phase ϕ_b sweep simulation for a qubit with $\omega_0 = (2\pi)50$ MHz. The intensity plots are the Fourier spectra of the simulated time-dependent population $P(t)$ for the initial (and readout) state $|+\rangle$ for panel (a) and $|0\rangle$ for panels (b)–(f). (a) Both the ac field (along z) and bias field (along x) are linearly polarized with $\omega_s = (2\pi)375$ MHz, $\omega_b = \omega_s + \omega_0 = (2\pi)425$ MHz, $\phi_s = 0$, and $\Omega_b = \Omega_{sz} = (2\pi)10$ MHz. (b) Both the ac field (along z) and bias field (along x) are linearly polarized with $\omega_s = (2\pi)375$ MHz, $\omega_b = \omega_s + \omega_0 - \Omega = (2\pi)422$ MHz, $\phi_s = 0$, and $\Omega_b = \Omega_{sx} = (2\pi)10$ MHz. The spin-locking drive amplitude is $\Omega = (2\pi)3$ MHz. (c) The ac field (along z) is linearly polarized, and the bias field (in the x-y plane) is circularly polarized with the same parameters as in panel (b). (d) Both the ac field (along x) and bias field (along x) are linearly polarized with $\omega_b = \omega_s + \Omega$, $\omega_s = (2\pi)375$ MHz, $\phi_s = 0$, and $\Omega_b = \Omega_{sx} = (2\pi)10$ MHz. The spin-locking drive amplitude is $\Omega = (2\pi)3$ MHz. (e) Both the ac field (in the x-y plane) and bias field (in the x-y plane) are circularly polarized with the same parameters as in panel (d). (f) The ac field (along x) is linearly polarized, and the bias field (in the x-y plane) is circularly polarized with the same parameters as in panel (d). All the dashed lines are theoretical predictions derived from the multimode Floquet theory.

intuitive explanation of the evolution modes under the effective Hamiltonian. The Rabi oscillation induced by the effective signal, e.g., the Ω_{Tx} term in Hamiltonian $\bar{H}_I = \Omega\sigma_x/2 - \Omega_{Tx}\cos[\Omega t + (\phi_b - \phi_s)]\sigma_z$, can be analyzed in a second rotating frame defined by the spin-locking field $\Omega\sigma_x/2$, where a static signal in the y-z plane $(\Omega_{Tx}/2)[\sin(\phi_b - \phi_s)\sigma_y - \cos(\phi_b - \phi_s)\sigma_z]$, arising from the effective target signal, induces spin precession with a rate Ω_{Tx} (or Ω_{Tz} for a longitudinal signal), which can be directly measured by monitoring the population in $|+\rangle$. However, when monitoring the evolution with an observation operator σ_z noncommuting with the rotating-frame transformation $(\Omega/2)\sigma_x$, we are able to see a mixture of the Rabi frequency and the rotating-frame frequency $\Omega \pm \Omega_{Tx,Tz}, \Omega$ in the Fourier spectra of the evolution, which form the Mollow triplet [37]. The intensity of the center band Ω and sidebands $\Omega \pm \Omega_{Tx,Tz}$ is determined by the initial state with respect to the direction of the static signal in the second rotating frame, which is then set by the initial phase $\phi_b - \phi_s$.

In Fig. 6, we simulate the evolution $P_{|0\rangle}(t)$ $[P_{|+\rangle}(t)$ for case 1 of longitudinal signal sensing in the lab frame] as a function of the phase ϕ_b (while keeping $\phi_s = 0$) for all six cases discussed in Appendix B and plot their Fourier spectra. When $\phi_b - \phi_s = 0$, the initial state is along the static target-field direction such that no spin precession is induced in the second rotating frame. Then, the evolution mode is simply an oscillation at the rotating-frame frequency Ω [or ω_0 for case 1 of longitudinal signal sensing in Fig. 6(a)], which corresponds to the Mollow center band. When $\phi_b - \phi_s = \pi/2$, the opposite behavior is observed, where the sidebands become most prominent and the center band vanishes. The vanishing of the center band here is due to the dynamical symmetry of the Hamiltonian, which is discussed in detail in Ref. [38]. When $\phi_b - \phi_s$ is an intermediate angle, the evolution mode is a mixture of both the center band and sidebands. These predictions are validated in detail in Fig. 6.

2. Effective Rabi frequency

To further validate the theoretical results of the effective target signal amplitudes $\Omega_T = \Omega_T(\omega_s, \omega_b, \Omega_s, \Omega_b)$ in the main text and Appendix B, we simulate the Rabi oscillations induced by the effective target signal as a function of these parameters and plot their Fourier spectra along with the theoretical predictions obtained in Eqs. (B2), (B10), and (B16) in Appendix B.

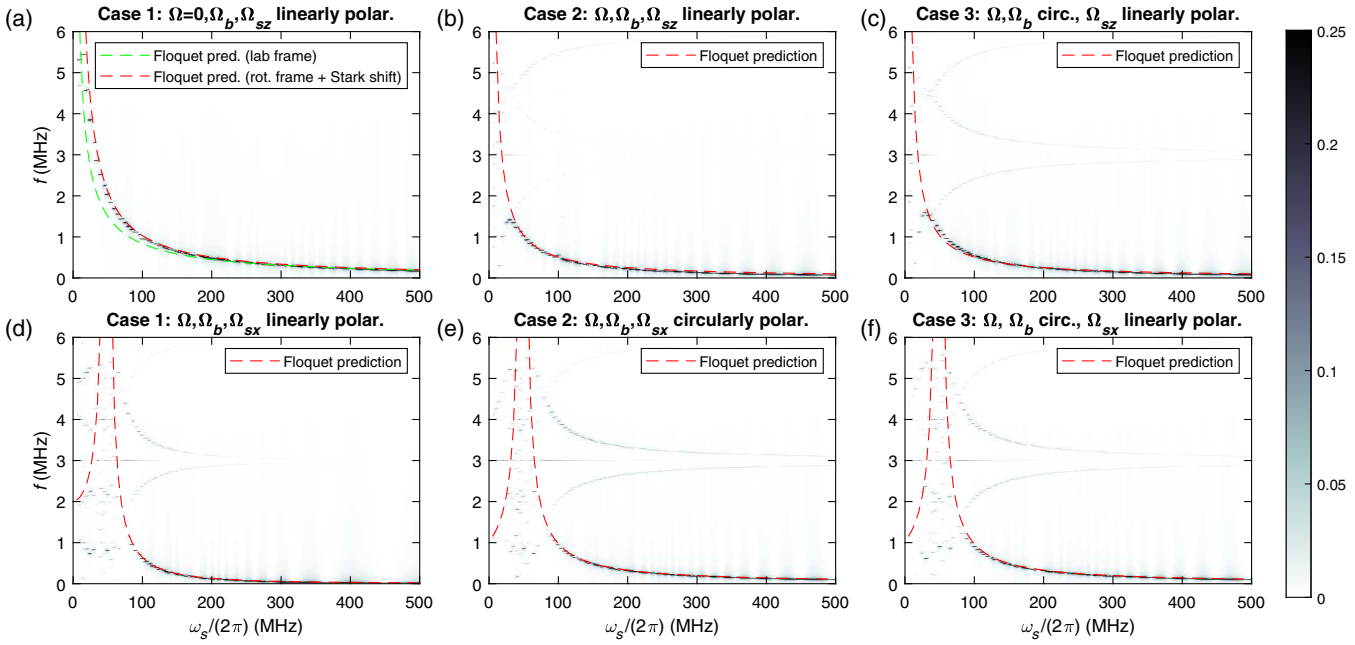

FIG. 7. Signal frequency ω_s sweep simulation. The parameters are the same as in Fig. 6 except for the phase $\phi_b = \pi/2$, initialization, and readout state $|+\rangle$ for panels (b)–(f), $|0\rangle$ for panel (a), and the signal frequency ω_s being swept. Resonance conditions $\omega_b = \omega_s + \omega_0$ (a), $\omega_b = \omega_s + \omega_0 - \Omega$ (b,c), and $\omega_b = \omega_s + \Omega$ (d)–(f) are satisfied when sweeping ω_s.

In Fig. 7, we simulate the Rabi oscillation spectrum as a function of the signal frequency ω_s for all six cases discussed in Appendix B in the ultrahigh-frequency range $\omega_s \gg \omega_0 = (2\pi)50$ MHz. The theoretical predictions are indicated by the dashed lines, which match well with the simulation. In Fig. 8, we use a large $\omega_0 = (2\pi)2200$ MHz to simulate an intermediate range $\omega_s < \omega_0$. The consistency between the theory and simulation demonstrates the broad applicable range of our theoretical approach.

In Fig. 9, we simulate the Rabi oscillation spectrum as a function of bias amplitude Ω_b. The theoretical predictions neglecting the ac Stark shift match well with the simulation

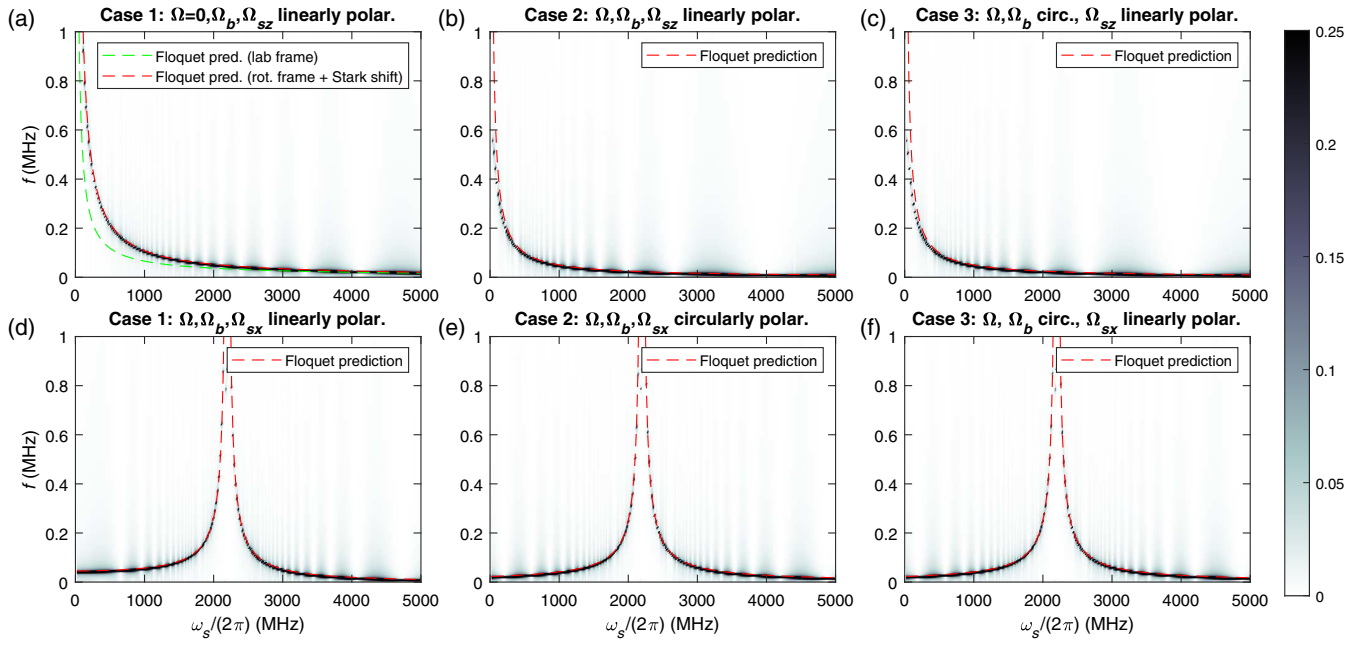

FIG. 8. Signal frequency ω_s sweep (intermediate frequency). The parameters are the same as in Fig. 7 except for the qubit energy $\omega_0 = (2\pi)2200$ MHz. Resonance conditions $\omega_b = \omega_s + \omega_0$ (a), $\omega_b = \omega_s + \omega_0 + \Omega$ (b,c), and $\omega_b = \omega_s + \Omega$ (d)–(f) are satisfied when sweeping ω_s.

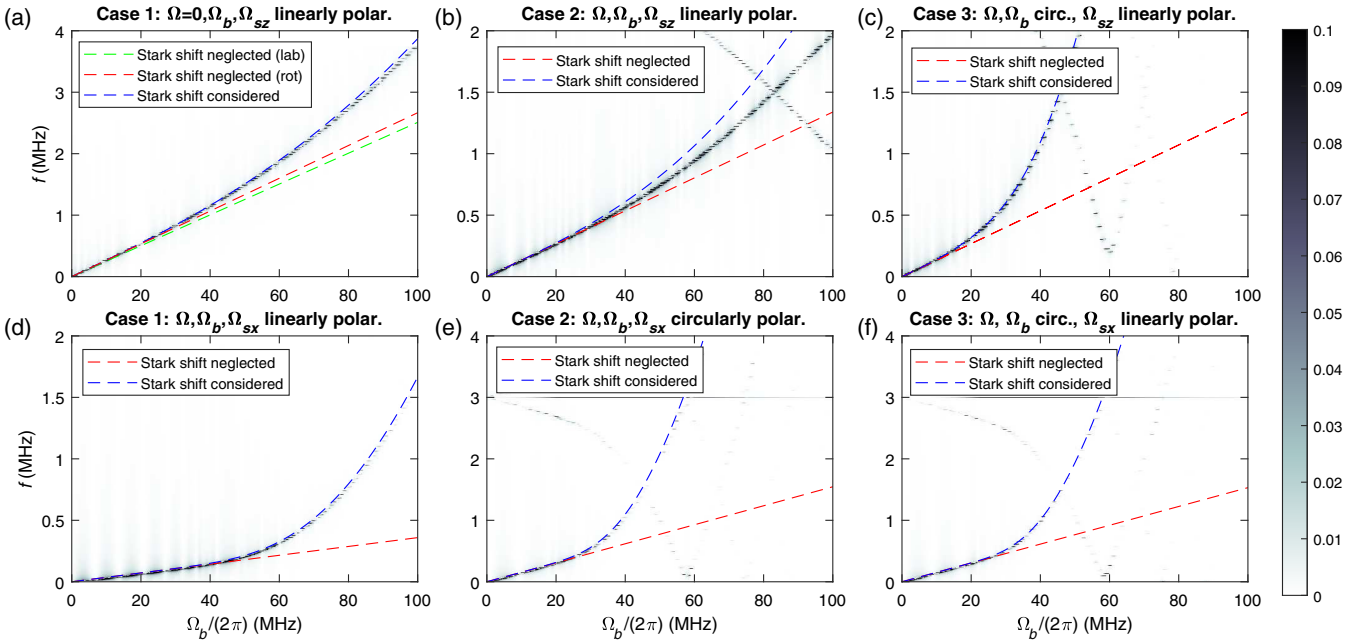

FIG. 9. Bias amplitude Ω_b sweep simulation. The parameters are the same as in Fig. 6 except for the phase $\phi_b = \pi/2$, initialization, and readout state $|+\rangle$ for panels (b)–(f), $|0\rangle$ for panel (a), and the bias amplitude Ω_b being swept. The same resonance conditions are satisfied as in Fig. 7. We note that in panel (b), the theoretical prediction considering the ac Stark shift deviates from the simulation earlier than other curves. This may be due to the unconsidered three-frequency mixing of the counterrotating term of the resonant spin-locking driving with $-2\omega_0$, the counterrotating term of the bias $\omega_b + \omega_0$, as well as the signal $-\omega_s$, which does not exist when both bias and resonant fields are circularly polarized in panel (c) or when $\Omega = 0$ in panel (a).

only when Ω_b is small, while the predictions considering the ac Stark shift match the simulation in a larger range.

In Figs. 7(a), 8(a), and 9, the theoretically predicted Rabi frequency is more precise when taking the ac Stark shift into account. See Supplemental Material [81] for detailed derivations of these theoretical analyses.

APPENDIX D: TIME DOMAIN ANALYSIS

In some specific cases, e.g., when both the bias and signal fields are along the transverse direction, there is a time-domain analysis that can also give the correct effective Hamiltonian under a reasonable approximation. One of the most popular methods is based on Jacobi-Anger expansion, which has been utilized to derive the system dynamics under periodic drives [42,69]. A detailed discussion is included in the Supplemental Material [81]. Here, we instead use an example (Protocol 3) to show that, by employing the typical method of calculating ac Stark shifts, we can also obtain the frequency-mixed signal under the condition $\omega_b, \omega_s \gg \omega_0$. We consider the sum of both the bias and signal fields in the lab frame

$$H_{bs} = [\Omega_s \cos(\omega_s t + \phi_s) + \Omega_b \cos(\omega_b t + \phi_b)]\sigma_x = \left[\alpha \cos\left(\frac{\omega_b + \omega_s}{2} t + \phi_c\right) + \beta \sin\left(\frac{\omega_b + \omega_s}{2} t + \phi_c\right)\right]\sigma_x, \tag{D1}$$

where $\phi_c = (\phi_b + \phi_s)/2$ and α, β are slowly varying envelopes of the fast oscillation at frequency $(\omega_b + \omega_s)/2$, with

$$\alpha = (\Omega_b + \Omega_s) \cos\left(\frac{\omega_b - \omega_s}{2} t + \frac{\phi_b - \phi_s}{2}\right), \tag{D2}$$

$$\beta = (-\Omega_b + \Omega_s) \sin\left(\frac{\omega_b - \omega_s}{2} t + \frac{\phi_b - \phi_s}{2}\right). \tag{D3}$$

Then, we can calculate the static ac Stark shift induced by both terms to obtain

$$\begin{aligned}\tilde{H}_{bs} &= -\frac{(\alpha^2 + \beta^2)\omega_0}{2[(\frac{\omega_b + \omega_s}{2})^2 - \omega_0^2]}\sigma_z \\ &= -\frac{\Omega_b^2 \omega_0}{2[(\frac{\omega_b + \omega_s}{2})^2 - \omega_0^2]}\sigma_z - \frac{\Omega_s^2 \omega_0}{2[(\frac{\omega_b + \omega_s}{2})^2 - \omega_0^2]}\sigma_z \\ &\quad - \frac{\Omega_b \Omega_s \omega_0}{(\frac{\omega_b + \omega_s}{2})^2 - \omega_0^2} \cos[(\omega_b - \omega_s)t + \phi_b - \phi_s]\sigma_z.\end{aligned} \tag{D4}$$

Here, the first two terms are the ac Stark shifts due to the bias and signal fields, and the third term, oscillating with a frequency $\omega_b - \omega_s$, is the frequency-mixed signal. Under the approximation $\omega_b, \omega_s \gg \omega_0$ and $\omega_b - \omega_s \sim \omega_0$, such a result is consistent with the Floquet derivation of Protocol 3 in Eq. (B16).

We note that for other protocols where the signal or bias field is not transverse, one can still use a similar analysis by properly choosing the reference frame and applying the ac Stark shift method or the Jacobi-Anger method, which should be analyzed case by case.

[1] J. C. Bardin, D. H. Slichter, and D. J. Reilly, *Microwaves in Quantum Computing*, IEEE J. Microwaves **1**, 403 (2021).

[2] F. Yan, S. Gustavsson, J. Bylander, X. Jin, F. Yoshihara, D. G. Cory, Y. Nakamura, T. P. Orlando, and W. D. Oliver, *Rotating-Frame Relaxation as a Noise Spectrum Analyser of a Superconducting Qubit Undergoing Driven Evolution*, Nat. Commun. **4**, 2337 (2013).

[3] N. Bar-Gill, L. Pham, C. Belthangady, D. Le Sage, P. Cappellaro, J. Maze, M. Lukin, A. Yacoby, and R. Walsworth, *Suppression of Spin-Bath Dynamics for Improved Coherence of Multi-Spin-Qubit Systems*, Nat. Commun. **3**, 858 (2012).

[4] F. Casola, T. van der Sar, and A. Yacoby, *Probing Condensed Matter Physics with Magnetometry Based on Nitrogen-Vacancy Centres in Diamond*, Nat. Rev. Mater. **3**, 17088 (2018).

[5] A. Yaghjian, *An Overview of Near-Field Antenna Measurements*, IEEE Trans. Antennas Propag. **34**, 30 (1986).

[6] D. A. Anderson, E. Paradis, G. Raithel, R. E. Sapiro, and C. L. Holloway, *High-Resolution Antenna Near-Field Imaging and Sub-THz Measurements with a Small Atomic Vapor-Cell Sensing Element*, in *2018 11th Global Symposium on Millimeter Waves (GSMM)* (2018), pp. 1–3, https://ieeexplore.ieee.org/document/8439437.

[7] K. Jomaa, F. Ndagijimana, H. Ayad, M. Fadlallah, and J. Jomaah, *Near-Field Characterization for 13.56 MHz RFID Antenna*, in *2017 International Symposium on Electromagnetic Compatibility—EMC* (2017), pp. 1–4, https://ieeexplore.ieee.org/document/8094759.

[8] C. T. Fancher, D. R. Scherer, M. C. S. John, and B. L. S. Marlow, *Rydberg Atom Electric Field Sensors for Communications and Sensing*, IEEE Transactions Quantum Eng. **2**, 1 (2021).

[9] D. H. Meyer, Z. A. Castillo, K. C. Cox, and P. D. Kunz, *Assessment of Rydberg Atoms for Wideband Electric Field Sensing*, J. Phys. B **53**, 034001 (2020).

[10] C. G. Wade, N. Šibalić, N. R. de Melo, J. M. Kondo, C. S. Adams, and K. J. Weatherill, *Real-Time Near-Field Terahertz Imaging with Atomic Optical Fluorescence*, Nat. Photonics **11**, 40 (2017).

[11] K. A. Gilmore, M. Affolter, R. J. Lewis-Swan, D. Barberena, E. Jordan, A. M. Rey, and J. J. Bollinger, *Quantum-Enhanced Sensing of Displacements and Electric Fields with Two-Dimensional Trapped-Ion Crystals*, Science **373**, 673 (2021).

[12] J. M. Taylor, P. Cappellaro, L. Childress, L. Jiang, D. Budker, P. R. Hemmer, A. Yacoby, R. Walsworth, and M. D. Lukin, *High-Sensitivity Diamond Magnetometer with Nanoscale Resolution*, Nat. Phys. **4**, 810 (2008).

[13] J. F. Barry, J. M. Schloss, E. Bauch, M. J. Turner, C. A. Hart, L. M. Pham, and R. L. Walsworth, *Sensitivity Optimization for NV-Diamond Magnetometry*, Rev. Mod. Phys. **92**, 015004 (2020).

[14] P. Wang, Z. Yuan, P. Huang, X. Rong, M. Wang, X. Xu, C. Duan, C. Ju, F. Shi, and J. Du, *High-Resolution Vector Microwave Magnetometry Based on Solid-State Spins in Diamond*, Nat. Commun. **6**, 6631 (2015).

[15] M. Loretz, T. Rosskopf, and C. L. Degen, *Radio-Frequency Magnetometry Using a Single Electron Spin*, Phys. Rev. Lett. **110**, 017602 (2013).

[16] A. Horsley, P. Appel, J. Wolters, J. Achard, A. Tallaire, P. Maletinsky, and P. Treutlein, *Microwave Device Characterization Using a Widefield Diamond Microscope*, Phys. Rev. Applied **10**, 044039 (2018).

[17] L. Shao, R. Liu, M. Zhang, A. V. Shneidman, X. Audier, M. Markham, H. Dhillon, D. J. Twitchen, Y.-F. Xiao, and M. Lončar, *Wide-Field Optical Microscopy of Microwave Fields Using Nitrogen-Vacancy Centers in Diamonds*, Adv. Opt. Mater. **4**, 1075 (2016).

[18] H. Y. Carr and E. M. Purcell, *Effects of Diffusion on Free Precession in Nuclear Magnetic Resonance Experiments*, Phys. Rev. **94**, 630 (1954).

[19] A. M. Souza, G. A. Álvarez, and D. Suter, *Robust Dynamical Decoupling*, Phil. Trans. R. Soc. A **370**, 4748 (2012).

[20] T. Joas, A. M. Waeber, G. Braunbeck, and F. Reinhard, *Quantum Sensing of Weak Radio-Frequency Signals by Pulsed Mollow Absorption Spectroscopy*, Nat. Commun. **8**, 964 (2017).

[21] J. Bylander, S. Gustavsson, F. Yan, F. Yoshihara, K. Harrabi, G. Fitch, D. G. Cory, Y. Nakamura, J.-S. Tsai, and W. D. Oliver, *Noise Spectroscopy through Dynamical Decoupling with a Superconducting Flux Qubit*, Nat. Phys. **7**, 565 (2011).

[22] G. T. Genov, N. Aharon, F. Jelezko, and A. Retzker, *Mixed Dynamical Decoupling*, Quantum Sci. Technol. **4**, 035010 (2019).

[23] M. W. Doherty, N. B. Manson, P. Delaney, F. Jelezko, J. Wrachtrup, and L. C. Hollenberg, *The Nitrogen-Vacancy Colour Centre in Diamond*, Phys. Rep. **528**, 1 (2013).

[24] S. A. Maas, *Microwave Mixers* (Artech House Publishers, Norwood, MA, 1986).

[25] J. H. Shirley, *Solution of the Schrödinger Equation with a Hamiltonian Periodic in Time*, Phys. Rev. **138**, B979 (1965).

[26] N. Goldman and J. Dalibard, *Periodically Driven Quantum Systems: Effective Hamiltonians and Engineered Gauge Fields*, Phys. Rev. X **4**, 031027 (2014).

[27] D. V. Else, B. Bauer, and C. Nayak, *Floquet Time Crystals*, Phys. Rev. Lett. **117**, 090402 (2016).

[28] D. V. Else, C. Monroe, C. Nayak, and N. Y. Yao, *Discrete Time Crystals*, Annu. Rev. Condens. Matter Phys. **11**, 467 (2020).

[29] A. Eckardt, *Colloquium: Atomic Quantum Gases in Periodically Driven Optical Lattices*, Rev. Mod. Phys. **89**, 011004 (2017).

[30] K. Wintersperger, C. Braun, F. N. Ünal, A. Eckardt, M. D. Liberto, N. Goldman, I. Bloch, and M. Aidelsburger, *Realization of an Anomalous Floquet Topological System with Ultracold Atoms*, Nat. Phys. **16**, 1058 (2020).

[31] N. H. Lindner, G. Refael, and V. Galitski, *Floquet Topological Insulator in Semiconductor Quantum Wells*, Nat. Phys. **7**, 490 (2011).

[32] A. G. Grushin, Á. Gómez-León, and T. Neupert, *Floquet Fractional Chern Insulators*, Phys. Rev. Lett. **112**, 156801 (2014).
[33] E. Boyers, P. J. D. Crowley, A. Chandran, and A. O. Sushkov, *Exploring 2D Synthetic Quantum Hall Physics with a Quasiperiodically Driven Qubit*, Phys. Rev. Lett. **125**, 160505 (2020).
[34] D. M. Long, P. J. D. Crowley, and A. Chandran, *Nonadiabatic Topological Energy Pumps with Quasiperiodic Driving*, Phys. Rev. Lett. **126**, 106805 (2021).
[35] D. M. Long, P. J. D. Crowley, and A. Chandran, *Many-Body Localization with Quasiperiodic Driving*, Phys. Rev. B **105**, 144204 (2022).
[36] M. Arnal, G. Chatelain, M. Martinez, N. Dupont, O. Giraud, D. Ullmo, B. Georgeot, G. Lemarié, J. Billy, and D. Guéry-Odelin, *Chaos-Assisted Tunneling Resonances in a Synthetic Floquet Superlattice*, Sci. Adv. **6**, eabc4886 (2020).
[37] G. Wang, Y.-X. Liu, and P. Cappellaro, *Observation of the High-Order Mollow Triplet by Quantum Mode Control with Concatenated Continuous Driving*, Phys. Rev. A **103**, 022415 (2021).
[38] G. Wang, C. Li, and P. Cappellaro, *Observation of Symmetry-Protected Selection Rules in Periodically Driven Quantum Systems*, Phys. Rev. Lett. **127**, 140604 (2021).
[39] Z. Shu, Y. Liu, Q. Cao, P. Yang, S. Zhang, M. B. Plenio, F. Jelezko, and J. Cai, *Observation of Floquet Raman Transition in a Driven Solid-State Spin System*, Phys. Rev. Lett. **121**, 210501 (2018).
[40] M. M. Roses, H. Landa, and E. G. Dalla Torre, *Simulating Long-Range Hopping with Periodically Driven Superconducting Qubits*, Phys. Rev. Research **3**, 033288 (2021).
[41] J. E. Lang, R. B. Liu, and T. S. Monteiro, *Dynamical-Decoupling-Based Quantum Sensing: Floquet Spectroscopy*, Phys. Rev. X **5**, 041016 (2015).
[42] M. Jiang, Y. Qin, X. Wang, Y. Wang, H. Su, X. Peng, and D. Budker, *Floquet Spin Amplification*, arXiv:2112.06190.
[43] M. Jiang, H. Su, Z. Wu, X. Peng, and D. Budker, *Floquet Maser*, Sci. Adv. **7**, eabe0719 (2021).
[44] H. Su, Y. Wang, M. Jiang, W. Ji, P. Fadeev, D. Hu, X. Peng, and D. Budker, *Search for Exotic Spin-Dependent Interactions with a Spin-Based Amplifier*, Sci. Adv. **7**, eabi9535 (2021).
[45] M. Jiang, H. Su, A. Garcon, X. Peng, and D. Budker, *Search for Axion-Like Dark Matter with Spin-Based Amplifiers*, Nat. Phys. **17**, 1402 (2021).
[46] I. Martin, G. Refael, and B. Halperin, *Topological Frequency Conversion in Strongly Driven Quantum Systems*, Phys. Rev. X **7**, 041008 (2017).
[47] S. Körber, L. Privitera, J. C. Budich, and B. Trauzettel, *Interacting Topological Frequency Converter*, Phys. Rev. Research **2**, 022023(R) (2020).
[48] D. Malz and A. Smith, *Topological Two-Dimensional Floquet Lattice on a Single Superconducting Qubit*, Phys. Rev. Lett. **126**, 163602 (2021).
[49] M. Leskes, P. Madhu, and S. Vega, *Floquet Theory in Solid-State Nuclear Magnetic Resonance*, Prog. Nucl. Magn. Reson. Spectrosc. **57**, 345 (2010).
[50] I. Scholz, B. H. Meier, and M. Ernst, *Operator-Based Triple-Mode Floquet Theory in Solid-State NMR*, J. Chem. Phys. **127**, 204504 (2007).
[51] I. Scholz, J. D. van Beek, and M. Ernst, *Operator-Based Floquet Theory in Solid-State NMR*, Solid State Nucl. Magn. Reson. **37**, 39 (2010).
[52] M. Ernst, A. Samoson, and B. H. Meier, *Decoupling and Recoupling Using Continuous-Wave Irradiation in Magic-Angle-Spinning Solid-State NMR: A Unified Description Using Bimodal Floquet Theory*, J. Chem. Phys. **123**, 064102 (2005).
[53] R. Gagliardi and S. Karp, *Optical Communications* (Wiley, New York, 1976).
[54] P. Krantz, M. Kjaergaard, F. Yan, T. P. Orlando, S. Gustavsson, and W. D. Oliver, *A Quantum Engineer's Guide to Superconducting Qubits*, Appl. Phys. Rev. **6**, 021318 (2019).
[55] P. Kumar, *Quantum Frequency Conversion*, Opt. Lett. **15**, 1476 (1990).
[56] P. Roelli, D. Martin-Cano, T. J. Kippenberg, and C. Galland, *Molecular Platform for Frequency Upconversion at the Single-Photon Level*, Phys. Rev. X **10**, 031057 (2020).
[57] J.-Q. Wang, Y.-H. Yang, M. Li, X.-X. Hu, J. B. Surya, X.-B. Xu, C.-H. Dong, G.-C. Guo, H. X. Tang, and C.-L. Zou, *Efficient Frequency Conversion in a Degenerate $\chi^{(2)}$ Microresonator*, Phys. Rev. Lett. **126**, 133601 (2021).
[58] P. Fisher, R. Cernansky, B. Haylock, and M. Lobino, *Single Photon Frequency Conversion for Frequency Multiplexed Quantum Networks in the Telecom Band*, Phys. Rev. Lett. **127**, 023602 (2021).
[59] G. Sinatkas, T. Christopoulos, O. Tsilipakos, and E. E. Kriezis, *Electro-Optic Modulation in Integrated Photonics*, J. Appl. Phys. **130**, 010901 (2021).
[60] R. G. Hunsperger, *Integrated Optics* (Springer, Berlin, Heidelberg, 1995).
[61] N. K. Langford, S. Ramelow, R. Prevedel, W. J. Munro, G. J. Milburn, and A. Zeilinger, *Efficient Quantum Computing Using Coherent Photon Conversion*, Nature (London) **478**, 360 (2011).
[62] S. Ramelow, A. Fedrizzi, A. Poppe, N. K. Langford, and A. Zeilinger, *Polarization-Entanglement-Conserving Frequency Conversion of Photons*, Phys. Rev. A **85**, 013845 (2012).
[63] D. Gottesman, T. Jennewein, and S. Croke, *Longer-Baseline Telescopes Using Quantum Repeaters*, Phys. Rev. Lett. **109**, 070503 (2012).
[64] L. Li, C.-L. Zou, V. V. Albert, S. Muralidharan, S. M. Girvin, and L. Jiang, *Cat Codes with Optimal Decoherence Suppression for a Lossy Bosonic Channel*, Phys. Rev. Lett. **119**, 030502 (2017).
[65] X. Guo, C. R. Breum, J. Borregaard, S. Izumi, M. V. Larsen, T. Gehring, M. Christandl, J. S. Neergaard-Nielsen, and U. L. Andersen, *Distributed Quantum Sensing in a Continuous-Variable Entangled Network*, Nat. Phys. **16**, 281 (2020).
[66] A. F. Linskens, I. Holleman, N. Dam, and J. Reuss, *Two-Photon Rabi Oscillations*, Phys. Rev. A **54**, 4854 (1996).
[67] M. Hirose, C. D. Aiello, and P. Cappellaro, *Continuous Dynamical Decoupling Magnetometry*, Phys. Rev. A **86**, 062320 (2012).
[68] G. Wang, Y.-X. Liu, Y. Zhu, and P. Cappellaro, *Nanoscale Vector ac Magnetometry with a Single Nitrogen-Vacancy Center in Diamond*, Nano Lett. **21**, 5143 (2021).

[69] Á. Gómez-León and G. Platero, *Designing Adiabatic Time Evolution from High-Frequency Bichromatic Sources*, Phys. Rev. Research **2**, 033412 (2020).

[70] G. Wang, Y.-X. Liu, and P. Cappellaro, *Coherence Protection and Decay Mechanism in Qubit Ensembles under Concatenated Continuous Driving*, New J. Phys. **22**, 123045 (2020).

[71] S. Meiboom and D. Gill, *Modified Spin-Echo Method for Measuring Nuclear Relaxation Times*, Rev. Sci. Instrum. **29**, 688 (1958).

[72] C. A. Ryan, J. S. Hodges, and D. G. Cory, *Robust Decoupling Techniques to Extend Quantum Coherence in Diamond*, Phys. Rev. Lett. **105**, 200402 (2010).

[73] B. J. Maertz, A. P. Wijnheijmer, G. D. Fuchs, M. E. Nowakowski, and D. D. Awschalom, *Vector Magnetic Field Microscopy Using Nitrogen Vacancy Centers in Diamond*, Appl. Phys. Lett. **96**, 092504 (2010).

[74] B. Chen, X. Hou, F. Ge, X. Zhang, Y. Ji, H. Li, P. Qian, Y. Wang, N. Xu, and J. Du, *Calibration-Free Vector Magnetometry Using Nitrogen-Vacancy Center in Diamond Integrated with Optical Vortex Beam*, Nano Lett. **20**, 8267 (2020).

[75] T. Weggler, C. Ganslmayer, F. Frank, T. Eilert, F. Jelezko, and J. Michaelis, *Determination of the Three-Dimensional Magnetic Field Vector Orientation with Nitrogen Vacancy Centers in Diamond*, Nano Lett. **20**, 2980 (2020).

[76] H. Zheng, Z. Sun, G. Chatzidrosos, C. Zhang, K. Nakamura, H. Sumiya, T. Ohshima, J. Isoya, J. Wrachtrup, A. Wickenbrock, and D. Budker, *Microwave-Free Vector Magnetometry with Nitrogen-Vacancy Centers along a Single Axis in Diamond*, Phys. Rev. Applied **13**, 044023 (2020).

[77] C. Zhang, H. Yuan, N. Zhang, L. Xu, J. Zhang, B. Li, and J. Fang, *Vector Magnetometer Based on Synchronous Manipulation of Nitrogen-Vacancy Centers in All Crystal Directions*, J. Phys. D **51**, 155102 (2018).

[78] D. Broadway, S. Lillie, S. Scholten, D. Rohner, N. Dontschuk, P. Maletinsky, J.-P. Tetienne, and L. Hollenberg, *Improved Current Density and Magnetization Reconstruction Through Vector Magnetic Field Measurements*, Phys. Rev. Applied **14**, 024076 (2020).

[79] J. M. Schloss, J. F. Barry, M. J. Turner, and R. L. Walsworth, *Simultaneous Broadband Vector Magnetometry Using Solid-State Spins*, Phys. Rev. Applied **10**, 034044 (2018).

[80] H. Clevenson, L. M. Pham, C. Teale, K. Johnson, D. Englund, and D. Braje, *Robust High-Dynamic-Range Vector Magnetometry with Nitrogen-Vacancy Centers in Diamond*, Appl. Phys. Lett. **112**, 252406 (2018).

[81] See Supplemental Material at http://link.aps.org/supplemental/10.1103/PhysRevX.12.021061 for more details on simulations and experiments.

[82] N. F. Ramsey, *A Molecular Beam Resonance Method with Separated Oscillating Fields*, Phys. Rev. **78**, 695 (1950).

[83] For a signal field $\vec{B}_{AC} = (B_x\hat{x} + B_y\hat{y} + B_z\hat{z})\cos(\omega_s t + \phi_s)$, this gives $\Omega_{sx,sy} = \gamma_e B_{x,y}/\sqrt{2}$ and $\Omega_{sz} = \gamma_e B_z/2$.

[84] E. Geva, R. Kosloff, and J. L. Skinner, *On the Relaxation of a Two-Level System Driven by a Strong Electromagnetic Field*, J. Chem. Phys. **102**, 8541 (1995).

[85] F. Yan, S. Gustavsson, J. Bylander, X. Jin, F. Yoshihara, D. G. Cory, Y. Nakamura, T. P. Orlando, and W. D. Oliver, *Rotating-Frame Relaxation as a Noise Spectrum Analyser of a Superconducting Qubit Undergoing Driven Evolution*, Nat. Commun. **4**, 2337 (2013).

[86] T. Wolf, P. Neumann, K. Nakamura, H. Sumiya, T. Ohshima, J. Isoya, and J. Wrachtrup, *Subpicotesla Diamond Magnetometry*, Phys. Rev. X **5**, 041001 (2015).

[87] R. Staacke, R. John, M. Kneiß, C. Osterkamp, S. Diziain, F. Jelezko, M. Grundmann, and J. Meijer, *Method of Full Polarization Control of Microwave Fields in a Scalable Transparent Structure for Spin Manipulation*, J. Appl. Phys. **128**, 194301 (2020).

[88] M. Oxborrow, J. D. Breeze, and N. M. Alford, *Room-Temperature Solid-State Maser*, Nature (London) **488**, 353 (2012).

[89] J. F. Barry, J. M. Schloss, E. Bauch, M. J. Turner, C. A. Hart, L. M. Pham, and R. L. Walsworth, *Sensitivity Optimization for NV-Diamond Magnetometry*, Rev. Mod. Phys. **92**, 015004 (2020).

[90] J. R. Maze, P. L. Stanwix, J. S. Hodges, S. Hong, J. M. Taylor, P. Cappellaro, L. Jiang, M. V. G. Dutt, E. Togan, A. S. Zibrov, A. Yacoby, R. L. Walsworth, and M. D. Lukin, *Nanoscale Magnetic Sensing with an Individual Electronic Spin in Diamond*, Nature (London) **455**, 644 (2008).

[91] G. Balasubramanian, I. Y. Chan, R. Kolesov, M. Al-Hmoud, J. Tisler, C. Shin, C. Kim, A. Wojcik, P. R. Hemmer, A. Krueger, T. Hanke, A. Leitenstorfer, R. Bratschitsch, F. Jelezko, and J. Wrachtrup, *Nanoscale Imaging Magnetometry with Diamond Spins under Ambient Conditions*, Nature (London) **455**, 648 (2008).

[92] J. M. Boss, K. S. Cujia, J. Zopes, and C. L. Degen, *Quantum Sensing with Arbitrary Frequency Resolution*, Science **356**, 837 (2017).

[93] T. Gefen, A. Rotem, and A. Retzker, *Overcoming Resolution Limits with Quantum Sensing*, Nat. Commun. **10**, 4992 (2019).

[94] C. Zhang, D. Dasari, M. Widmann, J. Meinel, V. Vorobyov, P. Kapitanova, E. Nenasheva, K. Nakamura, H. Sumiya, S. Onoda, J. Isoya, and J. Wrachtrup, *Quantum-Assisted Distortion-Free Audio Signal Sensing*, arXiv:2111.04100.

[95] A. A. Abdumalikov Jr, J. M. Fink, K. Juliusson, M. Pechal, S. Berger, A. Wallraff, and S. Filipp, *Experimental Realization of Non-Abelian Non-Adiabatic Geometric Gates*, Nature (London) **496**, 482 (2013).

[96] M. S. Rudner, N. H. Lindner, E. Berg, and M. Levin, *Anomalous Edge States and the Bulk-Edge Correspondence for Periodically Driven Two-Dimensional Systems*, Phys. Rev. X **3**, 031005 (2013).

[97] H. Primas, *Generalized Perturbation Theory in Operator Form*, Rev. Mod. Phys. **35**, 710 (1963).

[98] Note that the denominators in the third-order terms in Eq. (A17) are restricted to values $(n+n')\omega_q + (k+k')\omega_r = 0$ and $(n+n'')\omega_q + (k+k'')\omega_r \neq 0$.

[99] C. Foot, *Atomic Physics*, Oxford Master Series in Physics (Oxford University Press, New York, 2005).